American Mineralogist, Volume 108, pages 789–813, 2023

Eu speciation in apatite at 1 bar: An experimental study of valence-state partitioning by XANES, lattice strain, and Eu/Eu* in basaltic systems

Nicholas D. Tailby[1,2,*,†], Dustin Trail[3], E. Bruce Watson[2], Antonio Lanzirotti[4,‡], Matthew Newville[4], and Yanling Wang[3]

[1]Department of Earth and Planetary Sciences, American Museum of Natural History, Central Park West at 79th St., New York 10024-5192, U.S.A.
[2]Department of Earth and Environmental Sciences, Rensselaer Polytechnic Institute, Jonsson-Rowland Science Center, Troy, New York 12180, U.S.A.
[3]Department of Earth and Environmental Sciences, University of Rochester, Rochester, New York 14627, U.S.A.
[4]GSE-CARS, University of Chicago, Chicago, Illinois 60637, U.S.A.

Abstract

Partition coefficients for rare earth elements (REEs) between apatite and basaltic melt were determined as a function of oxygen fugacity (f_{O_2}; iron-wüstite to hematite-magnetite buffers) at 1 bar and between 1110 and 1175 °C. Apatite-melt partitioning data for REE^{3+} (La, Sm, Gd, Lu) show near constant values at all experimental conditions, while bulk Eu becomes more incompatible (with an increasing negative anomaly) with decreasing f_{O_2}. Experiments define three apatite calibrations that can theoretically be used as redox sensors. The first, a XANES calibration that directly measures Eu valence in apatite, requires saturation at similar temperature-composition conditions to experiments and is defined by:

$$\left(\frac{Eu^{3+}}{\sum Eu}\right)_{Apatite} = \frac{1}{1+10^{-0.10\pm0.01\times\log\left(f_{O_2}\right)-1.63\pm0.16}}.$$

The second technique involves analysis of Sm, Eu, and Gd in both apatite and coexisting basaltic melt (glass), and is defined by:

$$\left(\frac{Eu}{Eu^*}\right)_D^{\sqrt{Sm\times Gd}} = \frac{1}{1+10^{-0.15\pm0.03\times\log\left(f_{O_2}\right)-2.46\pm0.41}}.$$

The third technique is based on the lattice strain model and also requires analysis of REE in both apatite and basalt. This calibration is defined by

$$\left(\frac{Eu}{Eu^*}\right)_D^{\text{lattice strain}} = \frac{1}{1+10^{-0.20\pm0.03\times\log\left(f_{O_2}\right)-3.03\pm0.42}}.$$

The Eu valence-state partitioning techniques based on ($\sqrt{Sm\times Gd}$) and lattice strain are virtually indistinguishable, such that either methodology is valid. Application of any of these calibrations is best carried out in systems where both apatite and coexisting glass are present and in direct contact with one another. In holocrystalline rocks, whole rock analyses can be used as a guide to melt composition, but considerations and corrections must be made to either the lattice strain or $\sqrt{Sm\times Gd}$ techniques to ensure that the effect of plagioclase crystallization either prior to or during apatite growth can be removed. Similarly, if the melt source has an inherited either a positive or negative Eu anomaly, appropriate corrections must also be made to lattice strain or $\sqrt{(Sm\times Gd)}$ techniques that are based on whole rock analyses. This being the case, if apatite is primary and saturates from the parent melt early during the crystallization sequence, these corrections may be minimal.

The partition coefficients for the REE between apatite and melt range from a maximum $D_{Eu^{3+}} = 1.67 \pm 0.25$ (as determined by lattice strain) to $D_{Lu^{3+}} = 0.69 \pm 0.10$. The REE partition coefficient pattern, as observed in the Onuma diagram, is in a fortuitous situation where the most compatible REE (Eu^{3+}) is also the polyvalent element used to monitor f_{O_2}. These experiments provide a quantitative means of assessing Eu anomalies in apatite and how they be used to constrain the oxygen fugacity of silicate melts.

Keywords: Apatite, europium, Eu/Eu*, XANES, oxygen fugacity, f_{O_2}, valence, anomaly, KREEP, basalt, lunar, merrillite; Experimental Halogens in Honor of Jim Webster

* Present address: Division of Earth Science, School of Environmental and Rural Science, University of New England, Armidale, NSW, Australia. E-mail: ntailby@une.edu.au. Orcid 0000-0002-2305-3338
† Special collection papers can be found online at http://www.minsocam.org/MSA/AmMin/special-collections.html.
‡ Orcid 0000-0002-7597-5924

Introduction

The similar valence state observed among the rare earth elements (REE), along with systematically decreasing the ionic radii from La to Lu, lead to a generally coherent behavior for this group of elements, with predicable features in silicate melts and minerals (Trail et al. 2012; Burnham and Berry 2012). There are two notable exceptions: (1) Ce commonly shows a positive excursion and (2) Eu can show positive or negative excursions from an otherwise smooth trend when normalized to chondrite or host medium concentrations (noting that simultaneous positive Eu deviations and negative Ce deviations are also possible in certain natural systems; for examples see Hoskin and Schaltegger (2003); Trail et al. (2015); Kato et al. (2002); Elderfield et al. (1981); Plank and Langmuir (1998). These positive and/or negative excursions, generally known as anomalies, occur because Ce and Eu exhibit polyvalent behavior over the oxygen fugacity (f_{O_2}) range observed in the terrestrial bodies (e.g., Earth, Moon, Mars, Vesta). Here we focus on apatite-basalt partitioning of Eu species (Eu^{2+} and Eu^{3+}) to calibrate a new apatite redox (f_{O_2}) sensor. As the two Eu valence species show notably different ionic radii ($^{[VI]}Eu^{2+}$ = 1.17 Å and $^{[VI]}Eu^{3+}$ = 0.947 Å), it is not surprising that the two can have different partition coefficients between basalt and a crystallizing phase—making Eu and REE partitioning a potentially useful redox sensor among magmatic systems.

Recent studies into the pyroxene-basalt system (Karner et al. 2010) have provided an Eu^{2+}:Eu^{3+} XANES valence calibration for augite and a synthetic Martian basalt, while the works of Trail et al. (2011, 2012) and Burnham and Berry (2012) extended the use of Eu valence calibrations to zircon.

The use of apatite as a redox sensor is highly advantageous because, like zircon, apatite saturation has been shown to depend on key variables in silicate melts [e.g., P_2O_5, SiO_2, and temperature (Watson 1979; Tollari et al. 2006)]. Partitioning data for the trivalent REE^{3+} (particularly La, Pr, Sm, Gd, Dy, and Lu) has also been constrained between apatite-silicate and apatite-carbonatite systems (Watson and Green 1981; Klemme and Dalpé 2003), providing a basic knowledge of the trivalent Onuma diagram for apatite. Apatite, along with the merrillite-whitlockite group minerals, is also known to represent a dominant REE host within lunar basalts (Jolliff et al. 1993), making it among the most suited to REE valence-based studies in basalts from terrestrial planets. Apatite has also been reported from a large range of rock types, of different ages, from many locations on the Moon (e.g., KREEP, mare basalt, anorthosites, etc.), Mars, and the eucrite parent body (i.e., Vesta), making any Eu valence calibration of potentially broad application.

The last decade of research into lunar apatite has seen an intense focus on the OH-F-Cl content of the mineral's column anion sites. Direct comparison to terrestrial apatite grains, for example, has led to different hypotheses regarding the original volatile content of the Moon (McCubbin et al. 2010a, 2010b, 2011; Boyce et al. 2010; Greenwood et al. 2011; Tartèse et al. 2013). Notably, thermodynamic considerations regarding the uptake of several volatile species into apatite have been linked to f_{O_2} (Patino-Douce and Roden 2006), and thus apatite volatile content models of the Moon would become more complete with well-constrained f_{O_2}s. The development of an apatite redox sensor can also be directly compared to other methods used to constrain f_{O_2} in various types of lunar magmas (Sato 1976; Delano 1990; Herd 2008; Wadhwa 2008), and as a means to cross check and evaluate redox preservation among different mineral phases from the Moon. The use of REE as a redox sensor in apatite has the added advantage that, unlike other elements/components found in apatite (e.g., OH, F, Cl, Sr, Pb, etc.), the REE diffusivities in apatite are among the slowest (Cherniak 2000). This makes the REE among the more likely elements within the mineral to preserve primary magmatic signatures. The calibration presented here can also be directly compared to results of the research of Konecke et al. (2017, 2019) and Brounce et al. (2019), which uses $S^{6+}/\Sigma S$ in apatite as a means to determine oxygen fugacity in silicate melts.

Background information

Use of the intensity of a negative Eu anomaly in apatite as a proxy for redox conditions requires an understanding of Eu valence behavior in a basaltic melt and the partitioning behavior between a silicate liquid and a coexisting mineral phase (e.g., apatite). The europium valence ratio within a silicate melt can be linked to f_{O_2} by the reaction:

$$EuO(melt) + ¼O_2 = EuO_{1.5}(melt). \quad (1)$$

The log of the equilibrium constant for the Equation 1 reaction can be expressed as:

$$\log K = \log \frac{X^{melt}_{Eu^{3+}O_{1.5}}}{X^{melt}_{Eu^{2+}O_{1.0}}} + \log \frac{\gamma^{melt}_{Eu^{3+}O_{1.5}}}{\gamma^{melt}_{Eu^{2+}O_{1.0}}} - \frac{1}{4}\log f_{O_2} \quad (2)$$

where, X is the mole fraction and γ is the activity coefficient. Assuming Henrian behavior, which is consistent with the low concentration of Eu within our experiments and natural systems, the activity coefficients can be considered constant. A modified equilibrium constant (K') for the silicate melt can be expressed by rearranging Equation 2 to give (Berry and O'Neill 2004; Burnham and Berry 2012; and Trail et al. 2012):

$$\frac{Eu^{3+}}{\sum Eu} = 1/\left(1+10^{\left(-x\log f_{O_2}\right)+\log K'}\right). \quad (3)$$

According to Equation 3, $Eu^{3+}/\Sigma Eu$ can be linked to $\log(f_{O_2})$ via a sigmoidal relationship, where "x" is proportional to the number of electrons associated with the reaction and "x" should be ~0.25 (as predicted from Eq. 1). For an apatite (or any mineral) coexisting with a silicate melt of mixed Eu valence, $\log(f_{O_2})$ can be evaluated by apatite-melt Eu^{2+}-Eu^{3+}partitioning. We use a series of experiments (equilibrated at specific T-f_{O_2} conditions) to constrain the functional form described in Equation 3 by three different methods.

Crystal chemical controls on REE partitioning

To appreciate how the redox calibrations relate to REE partitioning between apatite and melt, it is important to understand the substitution mechanisms and potential crystallographic sites within the apatite crystal structure that will influence REE parti-

tioning. The structure of apatite [(Online Materials[1] Fig. OM1; modeled after Hughes and Rakovan (2015)] can be described by the formula (Fleet and Pan 2002):

$$^{[VI+III]}Ca(1)_4{}^{[VII]}Ca(2)_6(PO_4)_6X_2 \quad (4)$$

where the roman numeral (in closed brackets) refers to site coordination, Ca(1) and Ca(2) correspond to specific calcium sites, and X refers to the column anion site (e.g., F^-, Cl^-, OH^-, S^{2-}). Studies from natural and experimentally grown apatite demonstrate that numerous coupled substitution mechanisms exist for the REE^{3+}, with the dominant substitution mechanisms including (Hughes et al. 1991; Hughes and Rakovan 2015):

$$REE^{3+} + SiO_4^{4-} = Ca^{2+} + PO_4^{3-} \quad (5)$$
$$REE^{3+} + M^+ = 2Ca^{2+} \quad (6)$$
$$REE^{3+} + X^{2-} = Ca^{2+} + F^- \quad (7)$$
$$2REE^{3+} + \square = 3Ca^{2+} \quad (8)$$

where, M = monovalent cation (e.g., Na^+), X = divalent anion groups (e.g., SO_4^{2-}), and $\square$ = vacancy. The substitution of Eu^{3+} and other REE^{3+} cations required to constrain Eu/Eu* (i.e., Sm^{3+} and Gd^{3+} for Eq. 13 or La^{3+} through Lu^{3+} for Eq. 14) likely requires some combination of one or more of the substitution mechanisms described by Equations 5–8.

The substitution of Eu^{2+} is far simpler than the REE^{3+} cations and can be described as:

$$Eu^{2+} = Ca^{2+}. \quad (9)$$

Measurement of Eu oxidation states: Method 1–XANES determination

The most direct measurement of $Eu^{3+}/\Sigma Eu$ (where $\Sigma Eu = Eu^{2+} + Eu^{3+}$) in apatite from experiments is obtained by monitoring spectral features that are dependent on, and are proportional to, Eu valence. Previous studies have used Eu L_3 X-ray absorption near edge structures (henceforth described as XANES) to constrain Eu valence in silicate melts (Cicconi et al. 2012; Burnham et al. 2015), a coexisting mineral and silicate melt (Karner et al. 2010; Shearer et al. 2006), or to study Eu valence variation within an individual mineral (Rakovan et al. 2001). The use of Eu L_3 XANES spectra to determine valence is based on the observation that the near-edge region shows notable white lines, corresponding to a $2p_{3/2} \rightarrow 5d$ transition, that are sensitive to the relative abundance of Eu^{2+} and Eu^{3+} components within the analytical volume. The Eu^{2+} compounds show a dominant Eu L_3 XANES white line at ~6975.5 eV with a peak intensity at ~2 arbitrary units, while Eu^{3+} compounds show a dominant white line at ~6983.3 eV with a peak intensity of ~3 arbitrary units. The intense white line observed in the Eu L_3 XANES spectra is fortunate, as the different valence absorption bands show significant energy separation (~7 eV) and make spectral deconvolution of different Eu valence species straight-forward. This work employs direct and in situ Eu L_3 XANES spectroscopy from synthetic apatite and basalt equilibrated at controlled temperature-(f_{O_2}) conditions. Spectral analysis from normalized XANES data, discussed further in the methods section of this paper, can be used to define an $Eu^{3+}/\Sigma Eu$-f_{O_2} calibration for basaltic apatite applicable to natural apatite grains that crystallize and equilibrate at temperatures equivalent to experiments presented here (e.g., 1110–1175 °C). The $Eu^{3+}/\Sigma Eu$ in apatite (coexisting with melt/glass) can be determined from the following equation (noting that an arc tangent is also used to model the edge step):

$$\left(\frac{Eu^{3+}}{\sum Eu}\right)_{Apatite} = \frac{\varphi_{6983.3\,eV}}{\left(\varphi_{6983.3\,eV} + \varphi_{6975.5\,eV}\right)} \quad (10)$$

where φ_x corresponds to the amplitude or area under the Gaussian curve at energy "x" eV (noting that peak shape is unit normalized such that peak height and area are proportional). This method of calculation can be applied without direct measurement of the coexisting glass, though it assumes crystallization in a melt of similar composition at temperatures described in experiments. In an ideal scenario, analysis of both apatite and coexisting glass can be used to evaluate equilibrium.

Measurement of Eu oxidation states: Method 2—Lattice strain calculation of $(Eu/Eu^*)_D$

Where direct valence determination is not possible (i.e., XANES), Eu partitioning behavior can be modeled against the partitioning of other trivalent rare earth elements present within experiments (henceforth labeled REE^{3+})—namely La, Ce, Sm, Gd and Lu. In the lattice strain technique, shown graphically in Figure 1a, the REE^{3+}-based Onuma diagram from individual experiments can be used to calculate a theoretical partition coefficient for Eu^{3+} ($D_{Eu^{3+}}^{apatite/basalt}$). The intensity of a negative Eu anomaly can be calculated from the difference between the measured Eu value from an experiment to the estimated Eu^{3+} partition coefficient from a lattice strain model based on the REE^{3+} in apatite from the same experiment [the intensity of this negative anomaly we henceforth label $(Eu/Eu^*)_D$].

The lattice strain model is defined as:

$$D_i = D_0 \cdot \exp\left[\frac{-4\pi E N_A\left[\frac{r_0}{2}(r_i - r_0)^2 + \frac{1}{3}(r_i - r_0)^3\right]}{RT}\right] \quad (11)$$

where D_i = the partition coefficient for the element in question, D_0 = strain-free or ideal radius partition coefficient for the cation site, E = Young's modulus, N_A = Avogadro's number, R = the universal gas constant, r_i = ionic radius for the element in question (in the coordination of the site in question), r_0 = ideal ionic radius for the cation site, and T = temperature (in K). The Eu/Eu* lattice strain model, labeled $[(Eu/Eu^*)_D^{lattice\ strain}]$, of Brice (1975) and Blundy and Wood (1994) was previously used to calculate REE partitioning between apatite and carbonatitic melt (Klemme and Dalpé 2003) and was also used by Burnham and Berry (2012) and Smythe and Brenan (2016) to calculate $Ce^{4+}/\Sigma Ce$ or Ce/Ce* (i.e., similar redox-dependent valence behavior among other REE) between zircon and silicate melt. The equation used to describe the lattice strain calculated partitioning of Eu valence species is:

$$\left(\frac{Eu}{Eu^*}\right)_D^{lattice\ strain} = \frac{D_{Eu}^{Apatite/basalt}}{\left[D_{Eu^{3+}}^{\frac{Apatite}{basalt}}\right]_{lattice\ strain}} \quad (12)$$

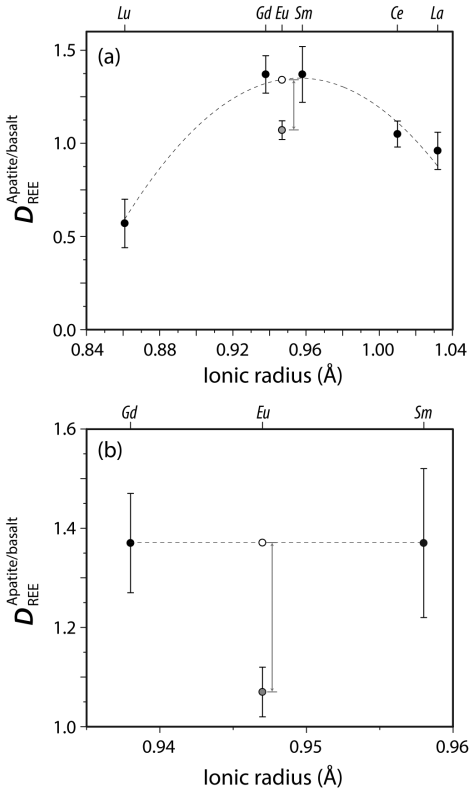

Figure 1. Demonstration of the two EPMA-based techniques used to calculate $(Eu/Eu^*)_D$ as shown from experiment ApREE-03b (Mo-MoO_2 buffer) and described by Equations 13 and 14. (**a**) The lattice strain parabola (dashed curve)—fit to La, Ce, Sm, Gd, and Lu data—can be used to constrain the partition coefficient for Eu^{3+}; i.e., a scenario where only trivalent Eu is present in the silicate melt. $(Eu/Eu^*)_D$ is defined as the measured Eu content (gray circle) divided by the theoretical Eu^{3+} content of a monovalent Eu^{3+}-bearing system defined by the lattice strain parabola (white circle). (**b**) The $(Eu/Eu^*)_D$ defined by neighboring REE-Gd and Sm. The numerator, or $D_{Eu}^{apatite/basalt}$, is directly measured (gray circle), while the denominator, or $\left(\sqrt{D_{Sm}^{Apatite/basalt} \times D_{Gd}^{Apatite/basalt}}\right)$(white symbol), is calculated from Sm and Gd measurements. In this type of calculation $(Eu/Eu^*)_D$ is represented by the ratio defined by gray arrow between numerator and denominator. All black symbols correspond to isovalent elements measured from this experiment (including Ce, as Ce^{4+} appears to be highly incompatible in apatite) that can be used to define the REE^{3+} Onuma diagram. Note that all ionic radii assume 6-coordination (see text, Klemme and Dalpé 2003 for details).

Measurement of Eu oxidation states: Method 3—$(Eu/Eu^*)_D$ calculated from neighboring Sm^{3+} and Gd^{3+}

The third calibration technique uses the intensity of the negative Eu anomaly (i.e., the negative excursion of $D_{Eu}^{apatite/basalt}$), relative to neighboring $D_{Sm}^{apatite/basalt}$ and $D_{Gd}^{apatite/basalt}$, determined by measuring coexisting apatite and glass. The theoretical partition coefficient for Eu^{3+} ($D_{Eu^{3+}}^{apatite/basalt}$) can be calculated from $\sqrt{D_{Sm}^{Apatite/basalt} \times D_{Gd}^{Apatite/basalt}}$. A graphic describing this method (Fig. 1) is henceforth labeled

$$\left[\left(\frac{Eu}{Eu^*}\right)_D^{\sqrt{Sm\times Gd}}\right]$$

and can be expressed:

$$\left[\left(\frac{Eu}{Eu^*}\right)_D^{\sqrt{Sm\times Gd}}\right] = \frac{D_{Eu}^{Apatite/basalt}}{\sqrt{D_{Sm}^{Apatite/basalt} D_{Gd}^{Apatite/basalt}}}. \quad (13)$$

Equations 12 and 13 are both examples where $(Eu/Eu^*)_D$ can be considered a proxy for $Eu^{3+}/\Sigma Eu$ in apatite. Methods 2 (Eq.12) and 3 (Eq. 13), unlike XANES methods, requires analysis of both apatite and coexisting glass.

Experimental methods

The parameters required to ensure apatite saturation within a basaltic melt at 1 bar (e.g., synthetic KREEP) have been previously evaluated (Watson 1979; Tollari et al. 2006) and the three dominant variables related to apatite saturation include P_2O_5 content (i.e., $a_{P_2O_5}^{basalt}$), SiO_2 content ($a_{SiO_2}^{basalt}$) and temperature (Watson 1979; and Tollari et al. 2006). The model of Watson (1979), for example, predicts a minimum P_2O_5 content of ~3.1 wt% to attain apatite saturation for a synthetic KREEP 15386 basalt at 1150 °C [where bulk SiO_2 = 50.83 wt% (Rhodes and Hubbard 1973)]. The calculated P_2O_5 content required for apatite saturation in experiments at temperatures from 1110–1175 °C containing ~50 wt% SiO_2 the melt will require approximately 3.1–3.5 wt% P_2O_5, and starting compositions were doped accordingly. While experiment temperatures are on the higher end of what would be expected to crystallize apatite in a natural systems, we choose these temperatures to produce crystals could be analyzable by XANES, with no or limited possibility of X-ray overlap/interaction with the coexisting glass.

The experimental starting material (Table 1) was modeled after Apollo sample KREEP 15386,1 considered to be an uncontaminated KREEP sample as interpreted from noble metal compositions (Warren et al. 1978). KREEP represents an excellent target composition because the elevated REE makes it the most suited for REE analysis, while the elevated P-content makes it the most likely system to saturate in apatite along the liquid line of descent. A 4 g starting mixture was synthesized by mechanical mixing of high-purity, reagent-grade powders of SiO_2 (α-Aesar, 99.8% purity), TiO_2 (α-Aesar, 99.9%), Al_2O_3 (α-Aesar, 99.98% purity), FeO (α-Aesar, 99.5% purity), $KAlSi_3O_8$ (α-Aesar), $NaAlSi_3O_8$(α-Aesar), $Ca_3(PO_4)_2$ (α-Aesar, >96.0% purity), Mg_2SiO_4 (α-Aesar), $CaSiO_3$ (α-Aesar, 99.0% purity), MgF_2 (α-Aesar, 99.99% purity), La_2O_3 (Spex), CeO_2 (Aldrich), Sm_2O_3 (REaction), Eu_2O_3 (REaction), Gd_2O_3 (REaction), Lu_2O_3 (Spex). This starting material is henceforth labeled as "syn-KREEP 15386-01a."

The REE starting mix is tailored to limit potential interferences in electron microprobe analysis, with a La:Ce:Pr:Sm:Eu:Gd:Lu weight ratio of 1:2:1:1:8:1:1. The REE concentration of the starting mix, ranging from 0.22–1.06 wt% REE^{3+}, is significantly higher than natural KREEP samples but is sufficiently low to maintain undersaturation in other phosphate phases like monazite, xenotime, etc. (which are never observed within experimental run products).

The starting mixture was ground under acetone in an agate mortar-pestle for 20 min, and then mechanically agitated in vials in a slowly rotating centrifuge at an orientation ~70° to the rotational axis for a minimum of 3 h. This process of "grinding and mechanical agitation" was then repeated three times. The synthetic starting powder was fired at 600 °C and then stored in a desiccator to ensure that the mixture remained nominally anhydrous.

Experiments were carried out in an evacuated SiO_2 tube suspended from an Al_2O_3 rod by a Pt wire and held within the hotspot of a 1 bar furnace. A type K thermocouple was held immediately adjacent to the experimental charge to ensure experiment temperatures are maintained to within ±5 °C (Fig. 2). Two different experimental approaches were used. The first employed a double capsule technique, where the buffer and experimental charge are separated by crushed SiO_2 chips. The second experimental technique employed a parti cipatory capsule (e.g., graphite or Mo metal or Fe metal), where the capsule also represents a component of the oxygen buffer within the charge. The bulk of experiments were carried out in AgPd capsules (14 experiments), with the exception of ApREE-01b (apatite capsule) and low-f_{O_2} runs ApREE-03b and ApREE-07b (Mo capsule), ApREE-09 and ApREE-12 (graphite capsule), and ApREE-06b (Fe capsule). As discussed later, all low-f_{O_2} capsules tend to result in lower Fe glasses due to a combination of alloying with the capsule (Mo capsules) and/or saturation in Fe-rich phases (e.g., olivine, schreibersite, etc.). The exception to this is experiment ApREE-06b (Fe-FeO), which saw considerable enrichment in Fe within the experimental glass (for this reason this experiment was not included in XANES analysis). In all experiments the top of the "syn-KREEP-15386-01a bearing" capsule remained open within the evacuated silica tube. As shown in Table 2 the experimental suite involved eight

Table 1. Major element and REE composition of natural and synthetic KREEP

	15386,19	15386,1	15386-01a[a]
		wt% oxide	
SiO_2	50.28	50.83	46.31
TiO_2	1.9	2.23	2.08
Al_2O_3	15.3	14.77	13.98
Cr_2O_3	0.36	0.31	n/i
FeO	10.2	10.55	9.6
MnO	0.15	0.16	n/i
MgO	10.5	8.17	7.77
CaO	9.5	9.71	12.23
Na_2O	0.81	0.73	0.74
K_2O	0.5	0.67	0.62
P_2O_5	n/a	0.7	3.62
F	n/a	n/a	0.6
		parts per million	
La	58	83.5	1950.2
Ce	147	211	3860.6
Sm	25.5	37.5	1936.1
Eu	2.4	2.72	9163.4
Gd	n/a	45.4	1926.1
Lu	2.48	n/a	2210.9

Notes: Error reported as 1σ. n/a = not analyzed. n/i = not included in starting mix.
[a] Synthetic starting material used in this study.

different solid-state f_{O_2} buffers (Fe_2O_3-Fe_3O_4, Ni-NiO, SiO_2-Fe_2SiO_4-Fe_3O_4, W-WO_2, FeO-Fe_3O_4, Fe-FeO, Mo-MoO_2, graphite-CO-CO_2). At completion, experiments were "drop quenched" in water to limit any post-experiment crystallization within the charge. Upon quenching, experiments were mounted in standard 1-inch epoxy rounds and polished to ¼ µm with colloidal silica. Optical and BSE imaging was used to determine the phases present within the experimental charge and to ensure the metal-metal oxide buffer was not exhausted during the experiment (Online Materials[1] Table OM2).

Analytical techniques

Energy-dispersive spectroscopy, back scattered electron, and cathodoluminescence mapping. Energy-dispersive spectroscopy and backscattered electron (BSE) imaging was performed on a Zeiss Evo 60 environmental SEM fitted with a LaB_6 crystal filament, housed at the American Museum of Natural History. All imaging was carried out at 10 keV and 30 nA. Cathodoluminescence (CL) imaging was carried out on a Gatan MonoCL attached to a Cameca SX100 electron microprobe, housed at the Rensselaer Polytechnic Institute. Analysis used an accelerating voltage of 15 kV and a beam current of 10 nA. The CL images in Figures 3e and 3f were obtained by combining spectra acquired through red (R), green (G), and blue (B) filters in Digital Micrograph software with equal weighing.

Electron microprobe analysis Major and minor element concentrations of experimental glasses and mineral phases (e.g., apatite, merrillite, plagioclase, and pyroxene) were acquired on a Cameca SX100 electron microprobe housed at the American Museum of Natural History. The analytical setup included 3 beam conditions and involved a sweep of 18 elements. The first condition was at 10 kV and 4 nA, involved 10 s counting times on F (LPC1) and Na (TAP) calibrated against MgF_2 and jadeite standards Initial analyses (experiments ApREE-01 to ApREE-04) did not include fluorine in the analytical routine. The second condition was at 15 keV and 20 nA with counting times of 20–30 s using for Ti, Mn, Ca, Mg, Al, P, and K (calibration standards include rutile, rhodonite, wollastonite, enstatite, K-feldspar, and berlinite). The third condition was at 15 keV and 30–40 nA using counting times of 30 s for Si and 200 s for La, Ce, Sm, Eu, Gd, and Lu calibrated against K-feldspar, $LaPO_4$, $CePO_4$, $SmPO_4$, $EuPO_4$, $GdPO_4$, and $LuPO_4$. The same three-condition, focused beam techniques were used for both mineral and glass analyses. Given the proximity of peak and background positions for neighboring lanthanides, peak and background positions were first modeled in Virtual WDS (Reed and Buckley 1998) and were compared with full wavelength scans from experimental apatites and REE phosphates standards on the LLIF spectrometer. The background peak positions (in sinθ) and average detection limits are for La (–600,+800; 734 ppm), Ce (–660,+660; 729 ppm), Sm (–650,+650; 663 ppm), Eu (–560,+720; 680 ppm), Gd (–500,+600; 704 ppm), Lu (–415,+595; 1146 ppm). Online Materials[1] Appendix OM3 provides details regarding the wavelength scans and peak/background positions used for WDS analysis.

The EPMA protocol involved analysis of between 4–6 apatite grains per experiment, with transects across individual crystals involving between 3–8 points, to evaluate the composition and variation among apatite populations from individual experiments. Elements Al, Si, Ti, and K were used to monitor signal contamination from glass or mineral inclusions within apatite. Durango and Wilberforce apatite standards were analyzed across all EPMA sessions, with measurements on the standard being made after approximately every 6 ApREE apatite analyses (i.e., every 1½ h). This Durango data was used to monitor any potential drift (none observed) and to evaluate accuracy of the REE data via comparison with the standard geochemistry information by Marks et al. (2012). A comparison of standard data can be found in Online Materials[1] Table OM5. Glass and apatite analyses from each experiment involved measurements obtained from two different regions of the capsule, though some capsules (e.g., ApREE-02a and ApREE-02b) have measurements from throughout the capsule (e.g., sequentially from four regions parallel to the long axis of the capsule) to investigate heterogeneity. Analysis from other phases from experiments (e.g., plagioclase, merrillite and pyroxene) are dependent on the size and distribution within experimental charges. Thin plagioclase laths presented a particular analytical challenge, and plagioclase compositions are not reported from experiments where the phase is too small for reliable analysis.

LA-ICP-MS. While the bulk of the geochemical data are based on EPMA and XANES analyses, we also include LA-ICP-MS analyses from 4 representative experiments (ApREE-03a, ApREE-03b, ApREE-07, ApREE-09). All LA-ICP-MS analyses were carried out on a Photon Machines 193 nm G2 laser systems equipped with a HelEx 2-volume sample chamber connected to an Agilent 7900 quadrupole mass spectrometer at the University of Rochester. Analysis involved two laser footprints (or "spot sizes"), the first involving a 3 µm spot for merrillite and apatite analysis and, the second involving a 20 µm circular spot for glass analysis. These

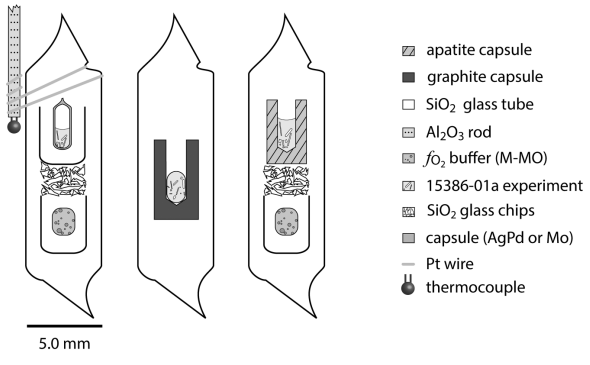

Figure 2. Experimental setup for ApREE experiments. Note that M-MO buffer represents a metal-metal oxide solid state f_{O_2} buffer (e.g., Ni-NiO). Note that left-hand and right-hand capsules include nested solid state buffers, while the middle experiment example includes a participatory buffer capsule (graphite).

Table 2. Experimental run conditions

Experiment no.	f_{O_2} buffer	log (f_{O_2})	T (°C)	Time (min)	Capsule	Run products
ApREE-01a	NNO	–8.02	1175	1380	AgPd	glass, ap, merr, plag
ApREE-01b	NNO	–8.02	1175	1380	Apatite	glass, ap, plag
ApREE-02a	IW	–12.26	1175	2660	AgPd	glass, ap, plag
ApREE-02b	IW	–12.26	1175	2660	AgPd	glass, ap
ApREE-03a	NNO	–8.31	1150	750	AgPd	glass, ap, merr, plag
ApREE-03b	MMO	–12.59	1150	750	Mo	glass, ap, plag, pyx
ApREE-04	HM	–3.28	1150	1145	AgPd	glass, merr, ap, plag
ApREE-06	QFM	–9.02	1150	720	AgPd	glass, ap
ApREE-06	IW	–12.59	1150	720	Fe	glass, ap, pyx
ApREE-07	HM	–3.28	1150	1500	AgPd	glass, ap
ApREE-07	MMO	–12.36	1150	1500	AgPd	glass, ap
ApREE-09	G-CO-CO_2	–14.51	1150	1275	Graphite	glass, ap, schrib
ApREE-12	G-CO-CO_2	–14.93	1110	1090	Graphite	glass, ap, plag, schrib
ApREE-12	NNO	–8.81	1110	1090	AgPd	glass, ap, plag, spinel
ApREE-12	WM	–10.63	1110	1090	AgPd	glass, ap, px
ApREE-13a	QFM	–9.53	1110	1590	AgPd	glass, ap
ApREE-13b	WWO	–11.83	1110	1590	AgPd	only melt
ApREE-15X	IW	–13.15	1110	1020	AgPd	glass, ap, plag
ApREE-15A-01	MMO	–12.97	1110	1020	AgPd	glass, ap, plag
ApREE-15A-02	MMO	–12.97	1110	1020	Ap	glass, ol, ap

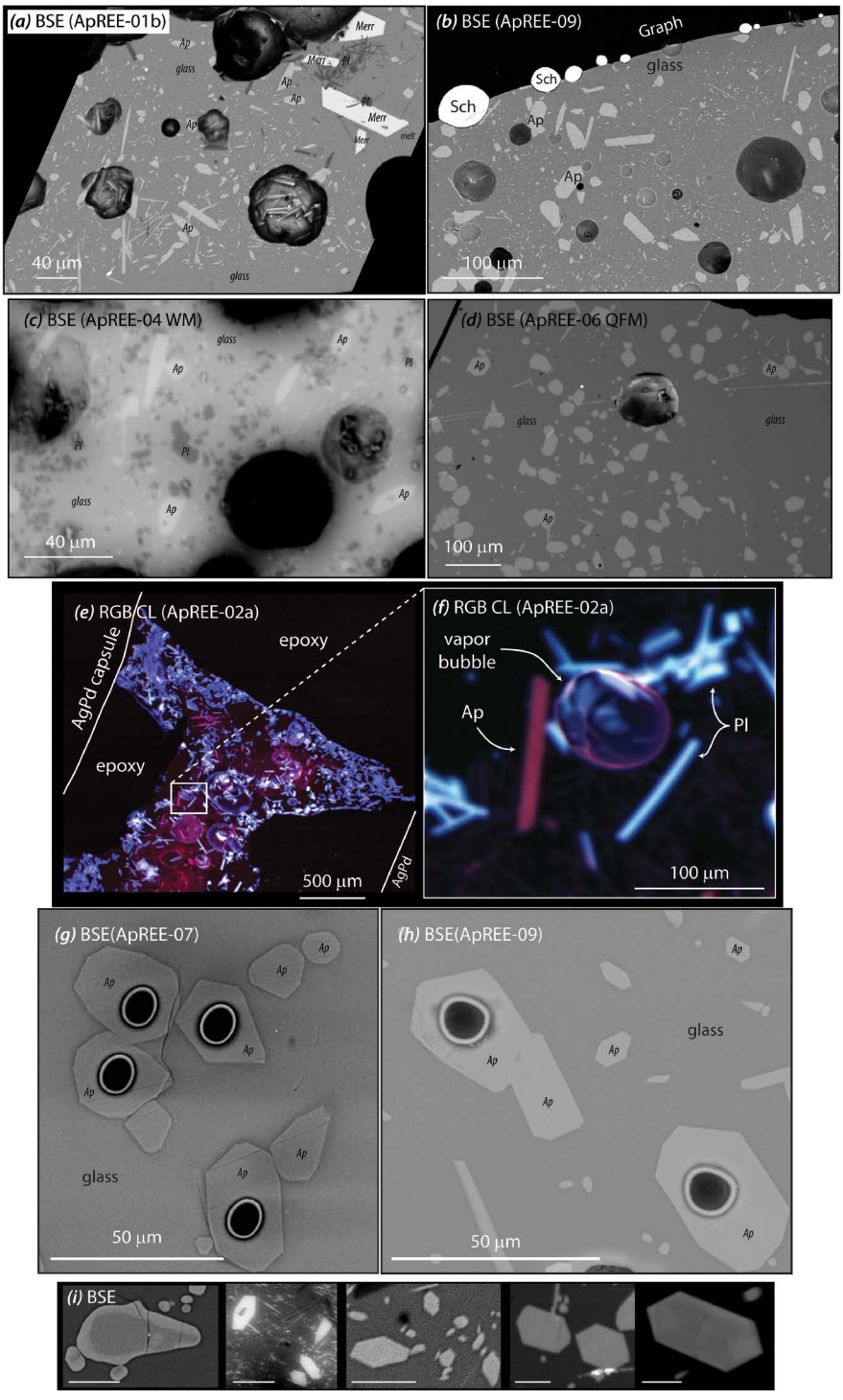

Figure 3. Representative photomicrographs of experimental run products. (**a**–**d**) BSE images from experiments; Ap = apatite; Pl = plagioclase feldspar; melt = basaltic glass; Sch = schreibersite; Merr = merrillite. (**e**–**f**) Cathodoluminescence (CL) image from combined red-green-blue (RGB) filters from experiment ApREE-02a. Note the different phases present within experimental charges are easily distinguished by the wavelength of luminescence (i.e., experimental plagioclase crystals tend to luminesce at blue wavelengths, while apatites luminesce at red wavelengths). (**g**–**h**) Representative BSE images taken over LA-ICP-MS spots from experimental runs, note: the locus of the laser spot within apatite crystals. (**i**) BSE or grayscale CL from apatite crystals from various experiments showing the crystal habit from left-to-right: ApREE-01b (NNO), ApREE-03 (WM), ApREE-01a (NNO), ApREE-06 (QFM), and ApREE-12 (WM). Scale bar for BSE images in **i** are all 20 µm. Note that all experiments, with the exception of ApREE-01b, which shows apatite seeds from the apatite capsule, show sharp euhedral habit indicative of equilibrium growth. (Color online.)

two analytical protocols employ a fluence of 4.72 J/cm^2 and a constant 7 Hz pulse rate over 16 s. At these conditions analysis involves a total of 105 laser pulses, with a 20 s pre-ablation background and a 30 s post-ablation background used in both types of analysis. The He flow rate in the sample chamber was set to 0.6 L/min, whereas the flow rate in the HelEx arm was 0.2 L/min.

All analysis employed a mass sweep comprised of ^{23}Na, ^{24}Mg, ^{29}Si, ^{31}P, ^{43}Ca, ^{139}La, ^{140}Ce, ^{147}Sm, ^{153}Eu, ^{157}Gd, and ^{175}Lu. Several masses (e.g., those corresponding to Na, Mg, Si, P, and Ca) are useful in terms of resolving clean spectra, such that mass ratios in the time-resolved spectra can be used to identify when apatite signal is contaminated by glass and vice versa. Given the small spot size, particularly during apatite/merrillite analysis, the locus of the LA-ICP-MS analyte was also imaged in BSE to ensure ablation pits are contained within the desired target material (see Figs. 3g and 3h).

NIST612 was used as the standard for glass analyses, USGS standard AGV-1 was used as a secondary standard. Silicon-29 was used as the internal standard for data reduction, as determined from EPMA analysis. The American Museum of Natural History Durango apatite standard (no. 41651) was used as the primary standard for apatite analysis (the same standard with detailed EPMA information presented in Online Materials[1] Table OM3), NIST612 was used as a secondary standard, and ^{43}Ca was used as an internal standard. Glass standards NIST612 and AGV-1 were measured for every 10 ApREE experimental glass analyses, while Durango apatite and NIST612 were measured for every 10 ApREE apatite/merrillite analyses. All data reduction was carried out in Iolite 3.1 software with background fit with a spline function (Paton et al. 2010, 2011).

XANES. Eu L_3 edge XANES spectra was collected at Beamline 13-ID-E (GSECARS), at the 7 GeV Advanced Photon Source, Argonne National Laboratory (Illinois, U.S.A.). Analyses of Eu-standards were collected on synthetic powders mounted in a thin film on Kapton tape and measured in transmission mode. These standards are of known valence and include $Eu^{2+}TiO_3$, $Eu^{3+}_2O_3$, $Eu^{3+}PO_4$, $Eu^{3+}Cl_3$, and $Eu^{3+}(NO_3)_3{\cdot}5H_2O$ (Fig. 4c). Analyses of ApREE experiments (Figs. 4a and 4b) were performed on the same 1- epoxy mounts used in EPMA. All XANES measurements were made prior to EPMA (and LA-ICP-MS analyses) to limit any potential damage to the apatite prior to X-ray measurements. No common apatite grains from an individual experiment were analyzed across analytical methods—this was done to limit any potential damage across techniques.

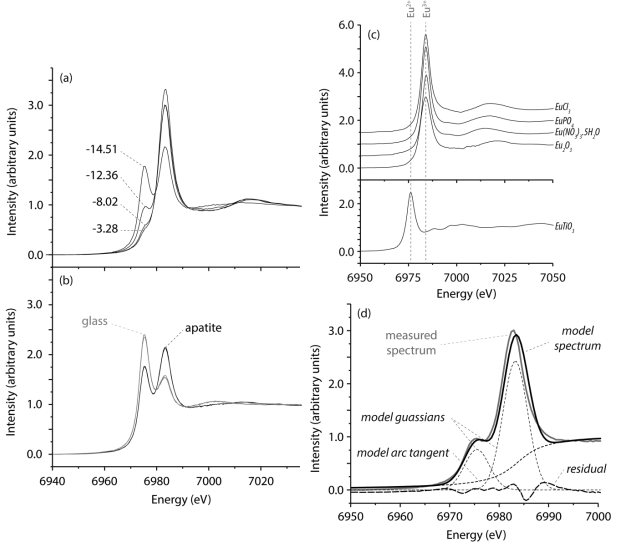

Figure 4. Normalized Eu L_3 XANES features from experiments. (**a**) Spectra from representative apatite experiments, where numerical values correspond to different log(f_{O_2}) defined in the experimental charge. (**b**) L_3 XANES spectra from coexisting glass (in gray) and apatite (in black) from experiment ApREE-07 [Mo-MoO$_2$, log(f_{O_2}) = –12.36]. (**c**) L_3 XANES spectra from standard Eu compounds measured in transmission mode. Note the dominant white line for Eu^{2+} (measured here on $EuTiO_3$) exists at lower energy (6975.5 eV) and normalized intensity (~2.5 arbitrary units) than Eu^{3+} compounds (here measured on $EuPO_4$, $EuCl_3$, $Eu(NO_3)_3{\cdot}5H_2O$, Eu_2O_3; with a normalized intensity between 3.0–3.5 arbitrary units). Note that individual Eu standards in **c** are stepped by 0.5 units for clarity. (**d**) Least squares regression from XANES spectrum from experiment ApREE-06 (QFM), where the edge-step is approximated by an arc tangent, Eu^{2+} and Eu^{3+} components are modeled as Gaussians and the residual are plotted.

The incident photon energy was selected via a cryogenically cooled Si-(111) double crystal monochromator and the energy resolution for measurements made at the Eu *K*-edge is ~0.5 eV. Energy calibration of the monochromator was carried out on the V *K*-edge and by defining the first derivative peak observed in a V metal foil spectrum at 5465 eV. The beam was located and focused to a 2 × 2 µm spot using Kirkpatrick-Baez (KB) mirrors by imaging on a Ce-doped $CdWO_4$ phosphor. The critical angle cut-offs of the mirrors on the instruments provided excellent rejection of high-energy harmonics. Absorption spectra were recorded from 6897–7115 eV, with steps of 5 (<6962 eV), 0.5 (6962–7007 eV), and ~3 eV (7007–7115 eV). Fluorescence was recorded at 45° to the sample and perpendicular to the incident X-ray beam using simultaneous counting and equal weighing on four Vortex-EX silicon drift detectors (SII NanoTechnology Inc.) from which the Eu L_3 integrated intensity was extracted and recorded. Reported analyses represent single points acquired using 3 s counting periods for a total analytical window of just under 7 min. Visual inspection and BSE observations of glass and apatite show no evidence for beam damage. Similar to 1-atmosphere experiments in mafic glasses carried out by Burnham and Berry (2014) on the Ce L_3-edge, this study did not see beam-induced changes in fluorescence intensity. This is supported by repeat analyses on common apatite crystals during rotation analyses, which saw no indication of fluorescence intensity change across the trio of measurements, nor any significant variation observed in the relative intensity of the Eu^{2+} and Eu^{3+} peaks (outside of that corresponding to mineral anisotropy).

The optical luminescence of apatite and merrillite under the X-ray beam makes it possible to actively image the footprint of the beam in real-time and identify regions within the experiment that are best suited to either mineral or glass analysis (see Fig. 5). Rapid "flyscan" X-ray fluorescence mapping of a region of interest (ROI) immediately surrounding a target material (typically involving energies corresponding to Eu$L\alpha$ line, Ca$K\alpha$ line, and Ti$K\alpha$ line; see Fig. 6), in addition to optical luminescence, provided an additional method for locating the mineral or melt regions most suited to analysis. These flyscan maps employed a 7.1 keV incident X-ray energy, with a 45 ms/pixel dwell time and a ROI defined by the target crystal.

The photon cross section for apatite can be calculated in Hephaestus (version 0.9.13; Ravel and Newville 2005). At the Eu L_3 edge (6977 eV) and at the average density of apatite (3.17 g/cm^3) a single-absorption length is 24.7 µm (though the majority of fluorescence X-rays recorded by the detector likely source from the near-surface environment) and as a general practice only grains that exceed twice this length were targeted (i.e., grains with a diameter ≥50 µm).

Two analytical approaches were used. The first involved analysis of randomly oriented apatite grains from throughout the experimental charge to evaluate the statistical variation within the experiment (Fig. 5c). Spectra using this approach were recorded from 28 apatite crystals from 9 experiments, 6 merrillite crystals from 1 experiment, and 20 glass locations from 9 experiments. Efforts were made to analyze plagioclase crystals from several experiments (notably ApREE-07 runs at HM and MMO), but the fine-grained plagioclase laths and the long absorption length at 6977 eV (24.6 µm) give rise to inconsistent results due to signal contamination from other coexisting phases.

The second approach involved orientation scans (relative to a reference or "north position" on the epoxy mount), with scans conducted at 0°, 60°, and 120° at a common point from four different grains within a given experiment. To accurately record the same position a rapid "flyscan" X-ray fluorescence mapping technique was used. This was done by identifying four target grains within an experiment at the 0° reference orientation, then linearly combining X-ray fluorescence maps with the Ti$K\alpha$, Ca$K\alpha$, and Eu$L\alpha$ lines. These three fluorescence lines can be combined to produce an RGB image that makes it possible to identify and distinguish regions of glass or apatite suitable for analysis while also helping target specific crystal (i.e., by visually confirming X-ray maps reproduce key features when rotated by a 60°). In Figure 5d, glass regions are generally represented by light blue hues while apatite grains are represented by red-pinkish hues. Analysis involving this approach includes 24 spectra, from eight apatite grains from two experiments. Once the initial fluorescence analyses are complete, the sample is then rotated to a 60° rotation and remapped in Ti-Ca-Eu space. The reference map and rotated map are directly compared (visually inspected) to ensure the same common grains and points are analyzed. Then fluorescence analyses are again carried out, though the new scans are at a 60° rotation to the original reference. Finally, the sample is rotated a further 60° (now 120° from the original orientation) and measured a final time.

The basic principle behind the two analytical techniques is that the first (analy-

ses at multiple locations within an experimental charge) provides a snapshot of the variation observed within a given phase within a given experiment, while the second (oriented scans) provides some quantitative estimate of affect of anisotropy on the Eu L_3 XANES spectra. In reality, the two techniques provide complementary information and should be evaluated as a whole, because they represent analyses from a common experiment.

Spectra normalizations were performed with Athena software (version 0.9.25, Ravel and Newville 2005) using the same set of normalization parameters for all spectra. Background subtraction over the pre-edge energy range employed a linear regression with clamps at 6915 and 6950 eV. The post-edge region involved regression with a quadratic polynomial with clamps at 7040 and 7175 eV. Visual inspection of the pre-edge and post-edge lines ensured that the energy range of pre-edge and post-edge lines were optimal for normalization.

As indicated in Figure 4d, Eu^{2+}:Eu^{3+} or $Eu^{3+}/\Sigma Eu$ were calculated using the "peak fitting" function in Athena (Ravel and Newville 2005) with the peak positions (energies) for spectral components fixed across all experiments. These fits involved Gaussian curves centered to absorption features at 6983.3 eV (Eu^{3+}) and 6975.5 eV (Eu^{2+}), with an arc tangent centered at 6983.8 eV (used to model the energy step), with the overall fitting region including 81 individual data points over a 45 eV energy range (6962–7007 eV). Analyses involved up to 6 measurements from individual apatite grains in random orientations and/or glass domains within the capsule, and error was calculated from the standard deviation across all measurements from an individual experiment. The orientation effect on spectra was not confirmed via individual grain rotations, but crystal habit does permit an evaluation of differences in $Eu^{3+}/\Sigma Eu$ for measurements carried out perpendicular vs. parallel to the apatite c-axis (Figs. 5a and 5b).

Results

Experimental products

Run products from experiments include phases that would be predicted from a Ca-rich KREEPy starting mix (equilibrated at 1 bar) at temperatures ranging from 1110 to 1175 °C. All experiments are saturated in apatite, with melts at lower temperature generally showing an increasing abundance of plagioclase and pyroxene. Crystallization of schreibersite at low f_{O_2} complicates use of the crystallization sequence in some experiments. Many experiments contain vapor bubbles, indicating the presence of one or more volatile species within the experimental charge. The simplest explanation is that volatile components within experiments attain a vapor pressure at experimental conditions (e.g., Na, F, K, P, CO, and CO_2). The alternative interpretation is that during water quenching H_2O was trapped within glasses. However, analytical totals approximate 100% and indicate a syn-KREEP experimental glasses are anhydrous glass.) If any water is present in experiments initially, volume expansion during heating to run temperature is likely to break the silica ampoule, making H_2O unlikely to be in any experiment). Even if minor amounts of water are contained within experiments, H_2O has a negligible influence on REE partitioning into apatite (Watson and Green 1981).

Apatite is euhedral in all experiments except one (see Fig. 3). As shown in Online Materials[1] Table OM1 all apatite grains are restricted to compositions close to end-member fluorapatite. The only exception is experiment ApREE-01b, which used an apatite capsule, where the observed apatite crystals show irregular and rounded crystal habits. The apatite grains from ApREE-01b also display observable zonation in CL (Fig. 3i, ApREE-01b), where dull BSE cores correspond to "seeds" from the Durango apatite capsule and bright rims correspond to new apatite growth.

In addition to apatite, phases present within experiments comprise variable mixtures of plagioclase and pyroxene, which become increasingly abundant in lower temperature experiments. The mineralogy and crystallization sequence observed in these experiments broadly match phase equilibria for the Ca-rich starting material reported in Walker et al. (1973), where apatite and plagioclase crystallization occur with decreasing temperature until the plagioclase-pyroxene cotectic is intercepted. Merrillite is also present in some experiments and is generally restricted to high temperature and high oxygen fugacity experiments (e.g., >1150 °C and f_{O_2} >NNO).

The experimental glass composition can generally be described as basaltic to picritic basalt, though low SiO_2 observed in experiments is the result of elevated P_2O_5 required for apatite saturation (Online Materials[1] Appendix OM4 and Table OM1). With progressive crystallization at lower, and saturation of different phases with changing f_{O_2} (namely schreibersite), melt composition can vary from experiment to experiment. Most importantly, and as seen by Drake (1972), the Fe content of experimental glass decreases with

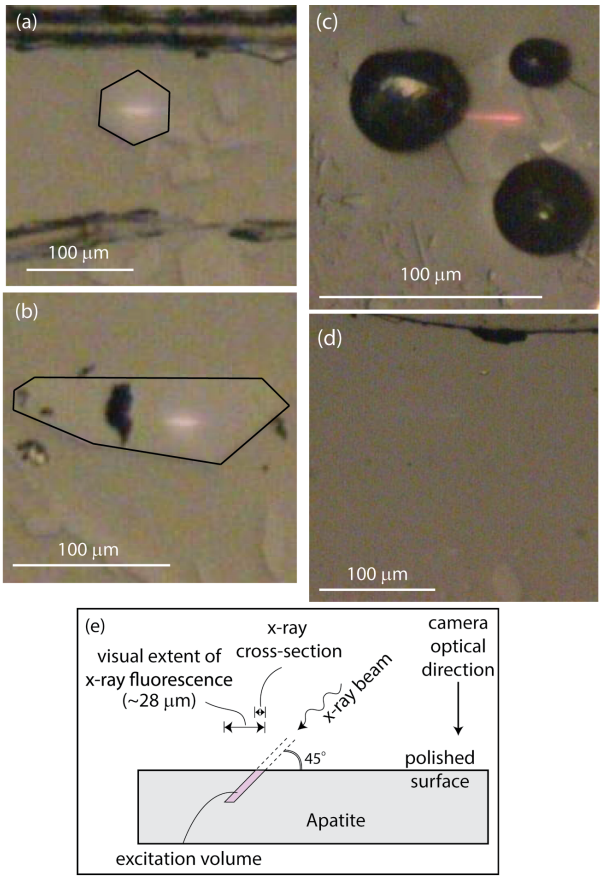

Figure 5. Optical luminescence observed from ApREE experiments, with the incident X-ray beam approaching the sample from 45° to the right. (**a**) Blue to purple luminescence observed within apatite crystal in ApREE-15X with analysis carried out on crystal polished perpendicular to the *c*-axis. (**b**) Blue luminescence from ApREE-15X conducted on apatite crystal near-parallel to the *c*-axis. (**c**) Red luminescence observed in merrillite from experiment ApREE-01a. (**d**) Very limited optical luminescence observed on glass from ApREE-09. (**e**) Diagram illustrating the relationship between the focused beam (2 × 2 μm at the crystal surface) and X-ray absorption path. The observed X-ray fluorescence in apatite/merrillite (~28 μm) is close to 2 absorption lengths (49.2/2 = 24.7 μm; where the division accounts for the 45° angle of the sample) as predicted by Hephaestus. (Color online.)

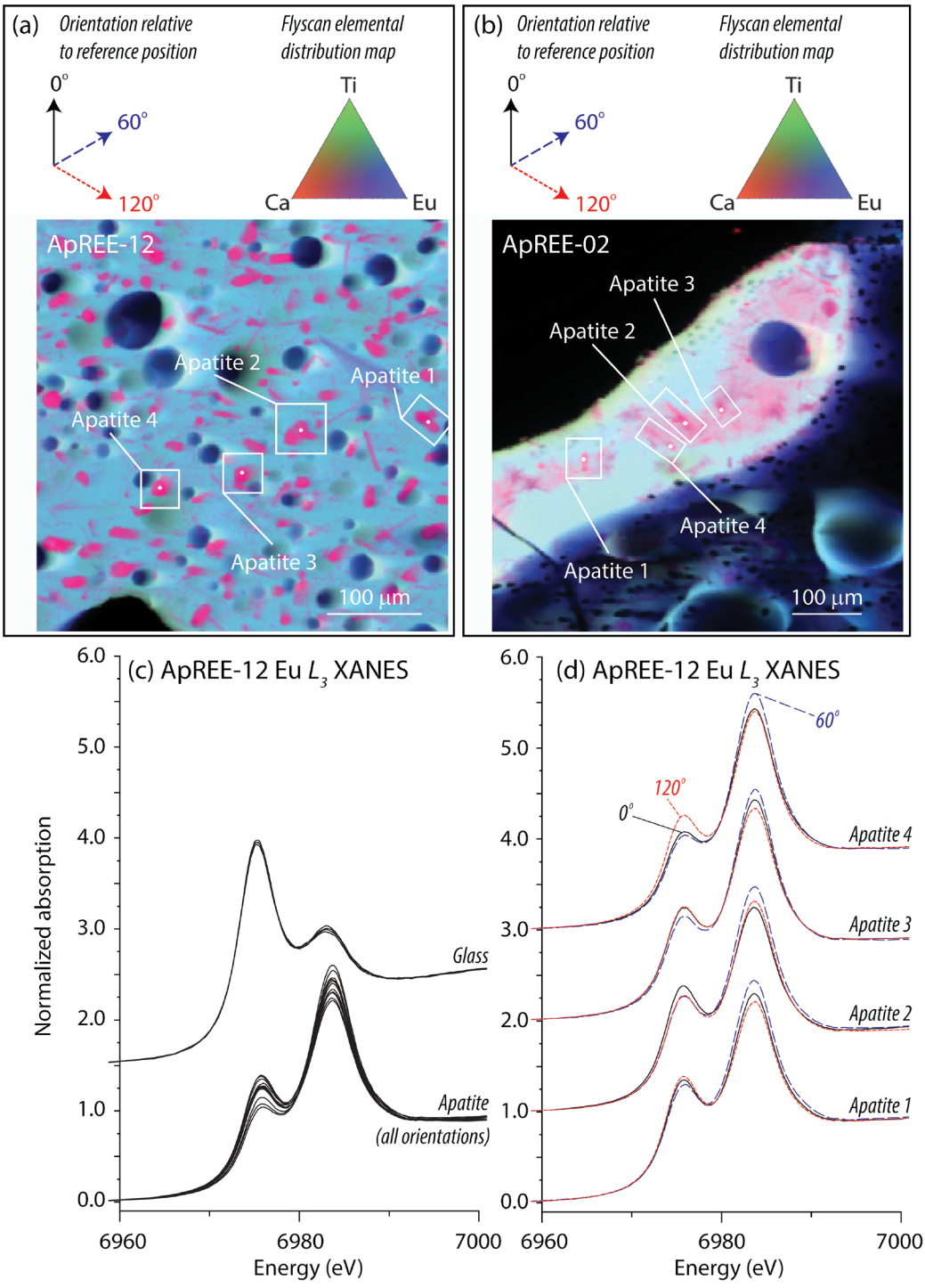

Figure 6. Representative and normalized EuL_3 XANES orientation scans from experiments (**a**) ApREE-12 and (**b**) ApREE-02. Reference orientation for flyscan image is at 0° (i.e., north position). Rotations indicated by arrows in **a** and **b** match color-coded spectra in **d**, with rotation indicated by arrows or degree symbols. RGB ternary image corresponds to X-ray fluorescence maps involving Ti$K\alpha$, Ca$K\alpha$, and Eu$L\alpha$ lines, making it possible to identify and distinguish regions of glass/apatite for analysis. Glass regions generally represented by light blue hues while apatite grains are represented by red-pinkish hues. EuL_3 XANES features from oriented experiments, where (**c**) corresponds to all glass and apatite analysis from experiment ApREE-12, and (**d**) corresponds to the four individual apatite crystals measured at the three reference orientations (0° in solid black curves, 60° in large dashed blue curves, and 120° in short red dashed curves). Note that the syn-KREEP 15386–01a glass records almost no observable orientation effect because it is isotropic, while apatite shows very minor variations due to the anisotropic nature of the crystal structure. (Color online.)

decreasing $\log(f_{O_2})$, particularly at $\log(f_{O_2}) < -12$ where schreibersite saturation is achieved. The metal-metal oxide solid state buffer can also influence glass/melt composition within experiments, as these components must attain some vapor pressure within the charge that enables chemical communication.

Cathodoluminescence

Apatite, merrillite, and plagioclase all luminesce under electron and X-ray beams (Mariano and King 1975; Roeder et al. 1987; Barbarand and Pagel 2001). This luminescence makes it possible to visually target glass domains that are free of small crystalline material. Many of the dominant phases present in the experimental charge luminesce at different wavelengths—e.g., apatite crystals are often seen as "red" while plagioclase commonly displays a "blue" luminescence—making it possible to distinguish regions within an experiment where two or more phases may be intergrown (Figs. 3e and 3f).

Electron microprobe analytical results

Average and 1σ uncertainties (in wt% oxide) for experimental run products, including apatite, glass and some additional run products are presented in Online Materials[1] OM1. The REE concentrations in experiment ApREE-01b (particularly La and Ce) are significantly different from "unseeded" experiments, suggesting that analytical totals are unreliable due to contamination from Durango apatite seeds in this experiment. Partitioning data from ApREE-01b are, therefore, not considered further. Faint sector zoning is noted from some experiments (Fig. 3i, ApREE-12; WM), but this variation is not accompanied by any detectable multimodality in minor or trace element data distribution (see Fig. 7 and discussion below). No inter-grain variation is observed in REE concentration within individual experiments, thus there appears to be no zonation depending on capsule position or crystal size.

Three experiments (ApREE-01a, ApREE-03a, ApREE-04) contain large, euhedral RE-merrillite (where RE indicates the phase is "rare earth" rich) crystals. These crystals are often also called whitlockite (or whitlockite group under Dana classification) and show some multiplicity among the different cation sites. Given that the experimental starting material was designed to be anhydrous and EPMA analytical totals are ~100% (Table 3; 100.55 ± 2.03, 99.98 ± 1.18), we conclude that these phosphates are members of the ~OH-free Merrillite family (e.g., Hughes et al. 2006; Jolliff et al. 2006). As shown in Figure 3a, the merrillite crystals show much higher BSE intensity relative to apatite, which is a good indication of the higher REE content of merrillite. The merrillite compositions are presented in Table 3 and generally show REE concentrations that are >1 wt% ΣREE (in wt% oxide), thus making the phase the dominant REE host within experiments. The calculated mineral compositions, based on 56 oxygen atoms, is $Ca_{16.8}REE_{1.5}(Mg,Fe)_{2.0}P_{13.7}Si_{0.2}O_{56}$ for ApREE-01a and $Ca_{16.5}REE_{1.6}(Mg,Fe)_{2.2}P_{13.7}Si_{0.6}O_{56}$ for ApREE-04—thus confirming saturation in an RE-Merrillite phase in ApREE-01a, ApREE-03a, and ApREE-04. See Online Materials[1] Table OM1a for melt composition.

In addition to apatite, merrillite, and glass analyses, attempts were made to obtain measurements from plagioclase and/or pyroxenes observed in experiments, but the REE concentrations were too low to be measured by EPMA (with the exception of experiments ApREE-01a, ApREE-02a, ApREE-04, and ApREE-15X, see Online Material Table OM1). Reliable plagioclase analysis is a particular problem, as the small size of laths makes it difficult to isolate an analytical volume suitable for EPMA. Experiments ApREE-15X and ApREE-02x show large Eu concentrations, while all other REE exist at concentrations below the detection limit; these experiments likely record a negative anomaly in apatite and have plagioclase with an associated positive anomaly.

LA-ICP-MS analytical results

Average and 1σ uncertainties (in wt% oxide) for experimental run products obtained from LA-ICP-MS analysis of a representative group of experiments, including values for apatite, glass and RE-merrillite are also presented in Online Materials[1] OM1a and OM1b (bottom). A representative apatite LA-ICP-MS spectra shows down hole decreases in counts

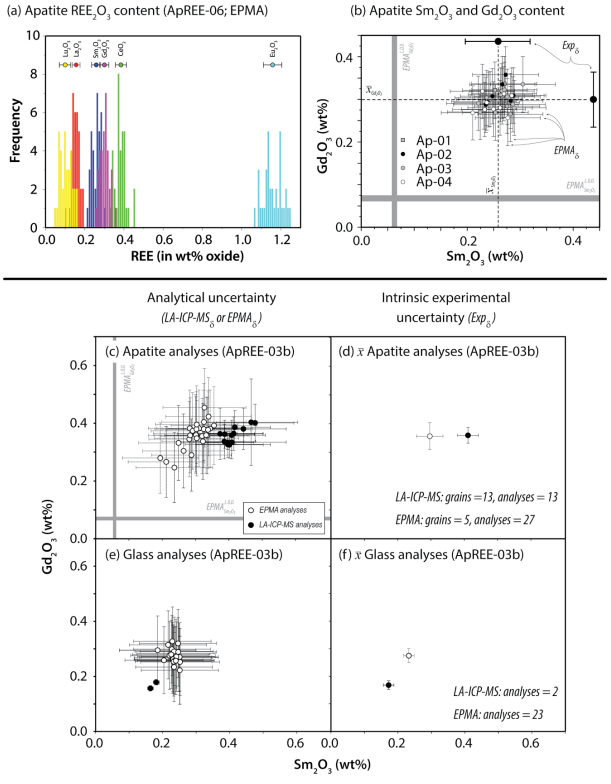

Figure 7. (**a**) Frequency distribution histograms for individual REE oxides based on 34 REE EPMA analyses from four apatite grains in experiment ApREE-06 (QFM). Note that each REE shows a normal distribution, with the average and 1σ projected. (**b**) Sm_2O_3 and Gd_2O_3 analyses from different synthetic apatite grains from experiment ApREE-06 (QFM). Different symbols correspond to analyses from a single grain, error bar in 1δ and gray shaded region corresponds to range of detection limit from all analyses. Note the clustering of data demonstrates almost no inter-grain variation in Gd- and Sm-content, arguably among the two most important elements when constraining Eu/Eu*, is observed in experiments. (**c** and **e**) Comparison of EPMA data (with analytical uncertainty; open circles with error bars) and LA-ICP-MS data (solid circles with error bars) for both apatite and glass. Note that EPMA detection limit as indicated and LA-ICP-MS detection limit (at parts per billion levels) essentially correspond to the origin of the graph. (**d** and **f**) Intrinsic, inter-grain or inter-glass uncertainty from repeat analyses from an experimental charge. (Color online.)

TABLE 3. Merrillite compositions in oxides and apfu from experiments

	ApREE-01a		ApREE-03a		ApREE-04	
n	24 (3)		48 (7)		15 (3)	
Composition (in wt% oxide)	oxide	δ	oxide	δ	oxide	δ
P_2O_5	42.9	2.03	42.65	0.94	41.46	1.62
SiO_2	0.55	0.02	0.65	0.34	1.5	1.02
Al_2O_3	0.02	0.01	0.21	0.6	0.21	0.3
FeO	0.34	0.05	0.65	0.06	0.36	0.14
MnO	bdl	–	bdl	–	bdl	–
MgO	3.45	0.06	3.57	0.13	3.85	0.14
CaO	41.54	0.18	41.36	0.77	40.36	0.49
Na_2O	0.05	0.03	0.05	0.03	0.08	0.02
TiO_2	bdl	–	bdl	–	0.04	0.03
K_2O	bdl	–	bdl	–	bdl	–
La_2O_3	1.08	0.04	1.11	0.06	1.06	0.05
Ce_2O_3	2.23	0.06	2.32	0.11	2.19	0.07
Sm_2O_3	1.26	0.04	1.26	0.07	1.26	0.03
Eu_2O_3	5.24	0.07	5.46	0.27	5.75	0.09
Gd_2O_3	1.47	0.05	1.42	0.09	1.46	0.04
Lu_2O_3	0.39	0.04	0.52	0.06	0.38	0.02
Cl	bdl	–	bdl	–	bdl	–
F	bdl	–	bdl	–	bdl	–
Total	100.55	2.03	101.3	1.16	99.98	1.18
Cations per 56 O atoms						
P	13.74		13.62		13.39	
Si	0.21		0.24		0.57	
$\Sigma(P,Si)_{tetra}$	13.95				13.96	
Al	bdl		0.09		0.09	
Ti	bdl		0.01		0.01	
Fe	0.11		0.2		0.11	
Mg	1.95		2.01		2.19	
Ca	16.84		16.72		16.49	
Na	0.04		0.04		0.06	
La	0.15		0.15		0.15	
Ce	0.31		0.32		0.31	
Sm	0.16		0.16		0.17	
Eu	0.68		0.7		0.75	
Gd	0.18		0.18		0.18	
Lu	0.04		0.06		0.04	
Σ(cations)	20.46		20.54		20.45	
Σ(REE)	1.53		1.58		1.6	
Σ(Mg,Fe)	2.05		2.21		2.3	

Notes: *n* = number of analyses (individual grains analyzed). $\Sigma(P,Si)_{tetra}$ = sum of phosphorus and silica on the tetrahedral site in merrillite (in apfu).

typical of our analytical session (Online Materials[1] Appendix OM3). Such data correspond to near-surface BSE image laser ablation spots (e.g., Figs. 3g and 3h), which show the dimension of the laser pit and the target phase. Collectively these two observations provide strong evidence that the analyses are of the target phase.

Individual analyses of REE concentrations of glass and apatite are remarkably similar to those reported from EPMA, and generally range from 950–13 000 ppm (by weight). While glass analyses from LA-ICP-MS have a much smaller error than EPMA measurements, apatite analyses across the two techniques are remarkably consistent for experiments at both high (i.e., hematite-magnetite buffer) and low-f_{O_2} conditions (i.e., graphite-CO-CO_2 or Mo-MoO_2 buffer).

TABLE 4. Comparison of apatite-melt experiments and experimental melt composition (wt%)

Reference	*P* (GPa)	*T* (°C)	SiO_2	Na_2O	H_2O
This study	1	1110–1175	39.7–50.2	0.2–0.8	0
Prowatke and Klemme	1	1250	35.9–61.5	1.3–16.8	0.0[a]
Watson and Green	0.75–2.0	950–1120	40.1–69.6	3.0–4.0	0.0–10.4

[a] The Prowatke and Klemme (2006) experiments contain no initial H_2O within the melt but hydroxyapatite within the starting material (i.e., a potential H_2O source).

XANES analytical results

Standard Eu compounds used (Fig. 4c) demonstrate that Eu^{2+}-compounds record a dominant Eu L_3 XANES feature (or white line) at 6975.5 eV, while Eu^{3+}-compounds record a dominant XANES feature at 6983.3 eV (note: XANES standard data can be made available by contacting the author). Data from spectral fits on apatite and glass (average and 1σ uncertainty) from a select number of individual experiments are reported in Table 6, while representative spectra from both apatite and glass are shown in Figures 4a and 4b.

As described in the methods, XANES data can be separated into two groups, where the first is used to provide a statistical snapshot of variation within an experiment through a data comparison of measurements collected at multiple locations within the experimental charge. The other group is used to investigate orientation effects.

The first method (analyses throughout the charge involving randomly oriented apatite grains) show that variations in $Eu^{3+}/\Sigma Eu$ are generally small in glass analyses (with σ varying from 0.0008–0.006 or 0.008–1.72%). Apatite analyses show higher standard deviations than glass, an observation consistent with the EPMA and LA-ICP-MS results and is likely related to the combined effect of anisotropy (a concern for both EPMA and XANES but not LA-ICP-MS) and intrinsic variations within apatite. The largest inter-grain variations in XANES analysis are observed in the most reduced experiments where the Eu^{2+} content reaches significant proportions (i.e., >13%)—most notably experiments ApREE-07 (Mo-MoO_2 buffer), ApREE-09 (C-CO-CO_2 buffer), and ApREE-15X (IW buffer)—where σ for $Eu^{3+}/\Sigma Eu$ are 2.75, 9.29, and 5.67% respectively. It is possible

TABLE 5. Lattice strain parameters derived from parabolic fits to Equation 5

Experiment	*T* (°C)	$\log(f_{O_2})$	*E* (GPa)	δ	r_0 (Å)	δ	$\ln(D_0)$	δ
This study—EPMA								
ApREE-01a	1175	–8.02	393	19	0.959	0.002	0.416	0.021
ApREE-03a	1150	–8.31	372	28	0.957	0.002	0.347	0.031
ApREE-03b	1150	–12.59	335	18	0.958	0.002	0.335	0.019
ApREE-04	1150	–3.28	337	25	0.962	0.003	0.285	0.027
ApREE-06	1150	–9.02	387	5	0.956	0	0.489	0.006
ApREE-06	1150	–12.59	391	4	0.96	0	0.824	0.004
ApREE-07	1150	–3.28	339	34	0.95	0.003	0.427	0.039
ApREE-07	1150	–12.36	313	22	0.968	0.003	0.663	0.023
ApREE-09	1150	–14.51	487	22	0.958	0.002	0.659	0.025
ApREE-12	1110	–14.93	366	11	0.959	0.001	0.673	0.012
ApREE-12	1110	–8.81	406	6	0.956	0	0.539	0.007
ApREE-13A	1110	–11.83	417	28	0.95	0.002	0.518	0.032
ApREE-15X	1110	–13.15	388	3	0.953	0	0.633	0.004
ApREE-15A-1	1110	–12.97	427	6	0.96	0.001	0.55	0.007
ApREE-15A-2	1110	–12.97	318	49	0.958	0.005	0.663	0.056
This study—LA-ICP-MS								
ApREE-03a	1150	–8.31	244	5	0.954	0.001	0.359	0.008
ApREE-03b	1150	–12.36	157	30	0.957	0.005	0.836	0.043
ApREE-07	1150	–3.28	293	9	0.953	0.012	0.427	0.172
ApREE-09	1150	–14.51	316	152	0.953	0.12	1.501	0.246
Average			352	25	0.957	0.009	0.587	0.041
Klemme and Dalpé (2003)								
BS19	1250	uc.	223	28	0.943	0.004	0.55	0.02
BS23	1250	uc.	321	95	0.94	0.01	0.5	0.05
BS25	1250	uc.	405	170	0.94	0.01	0.47	0.05
Average			316	97	0.941	0.008	0.507	0.04
Watson and Green (1981)								
818	1080	uc.	327	16	0.96	0.001	1.64	0.03
822	1120	uc.	385	4	0.952	<0.001	1.72	<0.01
Average			356	10	0.956	0.001	1.68	0.01

Notes: uc. = unconstrained (i.e., run at intrinsic oxygen fugacity of the experimental medium).

that some of this variation relates to crystallographic orientation effects on the in situ XANES method (a condition that would extend to calibration applications), but such variations only appear to influence the estimated totals by ~2–10%.

The second analytical technique involves oriented analyses from four apatite grains from representative experiments, at three 60° orientations. The orientation-dependent variation in calculated $Eu^{3+}/\Sigma Eu$ in repeat apatite analyses from experiment ApREE-02 ranges from 1.3–7.2%, while experiment ApREE-12 ranges from 3.0–7.9%. The oriented analyses show remarkably similar $Eu^{3+}/\Sigma Eu$ variations to those measured from numerous randomly oriented apatite grains using XANES methodology 1. ApREE-12 (C-CO-CO_2) and ApREE-02b (IW) represent examples where both Eu^{2+} and Eu^{3+} spectral features are abundant (i.e., the samples contain a mixture of Eu valence species), such that potential orientation-dependent spectral variation is maximized. In other words, if the maximum variation in orientation-dependent calculated $Eu^{3+}/\Sigma Eu$ is observed in the relative peak heights at $\varphi_{6975.5}$ and $\varphi_{6983.3}$, then by definition the largest variation must be observed at the inflection point of the valence speciation sigmoid curve. This variation will likely decrease systematically as one valence species (and one spectral feature) begins to dominate the system. The average, maximum observed orientation-dependent variation observed is 4.8 ± 2.2%, indicating that while apatite anisotropy can result in subtle changes to $\varphi_{6975.5}$:$\varphi_{6983.3}$ in the Eu L_3 XANES features, the influence of this effect can be measured and calculated using synchrotron-based techniques. For direct comparison of the two XANES analytical protocols see Figure 5c vs. 5d.

Discussion

An evaluation of EPMA data robustness and analytical considerations

The work by Laputina et al. (1999), Reed and Buckley (1998), Marks et al. (2012), and Henderson (2011) collectively demonstrate that use of the electron microprobe for the study of major, minor and trace elements in natural apatite—most notably the REEs—is possible when done properly and where concentration/s permit. This requires analytical protocols that take specific note of beam setup, orientation affects, background positions, potential overlap corrections and the use of appropriate standards. Interested readers are strongly encouraged to explore Online Materials[1] Appendix OM3 and Table OM5 section of this paper for further information. Previous studies into REE partitioning, most notably those involving the study of lunar phosphates (i.e., apatite, RE-merrillite), have largely used ion microprobe techniques (e.g., Jolliff et al. 1993; Shearer et al. 2011; Robinson et al. 2017). This is due to a combination of factors, including low concentration (i.e., ppm or lower concentrations), potential matrix mismatch between standards and unknowns (i.e., the use of REEs in glasses vs. REE-phosphates), and X-ray peak overlap issues among the various REE. The various issues that make lunar apatite analysis difficult have been almost entirely avoided by deliberately doping experiments at elevated concentrations. Experiments contain thousands of ppm of select REE while (rather than many of the REE existing at ppm or ppb in natural silicate-phosphate systems), while also avoiding the odd-even effect. The experimental approach also has the advantage that elevated REE concentrations are kept specifically low such that partitioning remains Henrian, and ensuring primary REE-bearing phase saturation (e.g., monazite or xenotime) is not achieved.

Our experiments were designed to avoid REEs that cause potential WDS overlaps that will influence either the lattice parabola or Sm:Eu:Gd (in either peak or background position), with the highest calculated overlap correction (VirtualWDS software: Reed and Buckley 1998) from any apatite, glass, or merrillite measurement being 0.00008% (see Online Materials[1] Table OM1).

It is important to emphasize how errors are calculated, as this will explain why the error bars associated with $[(Eu/Eu^*)_D^{\text{lattice strain}}]$ are larger than those of

$$\left(\frac{Eu}{Eu^*}\right)_D^{\sqrt{Sm\times Gd}}.$$

As an example, the error bars for individual data points from the apatite and silicate glass from ApREE-03b (mixed valence with a clear negative Eu anomaly) represent the standard deviation derived from the EPMA counting statistics (Figs. 8a and 8b). Note that the individual REE_2O_3 concentrations of apatite and glass reflect the La:Ce:Sm:Eu:Gd:Lu (1:2:1:1:8:1:1) ratio of the experiment. This odd REE shape makes it highly unlikely to replicate a lattice strain parabola by analytical artifacts, rather a parabola is only possible through the combined clean analysis of both apatite and glass.

As shown in Figure 8c the $D_{REE}^{\text{apatite/basalt}}$ an individual apatite within experiment ApREE-03b can collectively shift up or down in Sm, Eu, and Gd partitioning space. This collective shift results in an

$$\left(\frac{Eu}{Eu^*}\right)_D^{\sqrt{Sm\times Gd}}$$

that remains relatively consistent from grain to grain (or analysis to analysis), while the concentration-based variation in absolute partition coefficients may vary for individual REE. If we take 8 apatite-glass pairs from representative ApREE-03b experiment, and propagate through Sm, Eu, and Gd across all the apatite and glass data we calculate a

$$\left(\frac{Eu}{Eu^*}\right)_D^{\sqrt{Sm\times Gd}} = 0.74 \pm 0.06$$

(note these values are reported later in Figs. 14 and 15). If we simply take the

$$\left(\frac{Eu}{Eu^*}\right)_D^{\sqrt{Sm\times Gd}}$$

from the 8 apatite-glass pairs and look at the variation among that population (rather than propagating error through Sm, Eu, and Gd across all apatite and glass analyses), then

$$\left(\frac{Eu}{Eu^*}\right)_D^{\sqrt{Sm\times Gd}} = 0.74 \pm 0.04$$

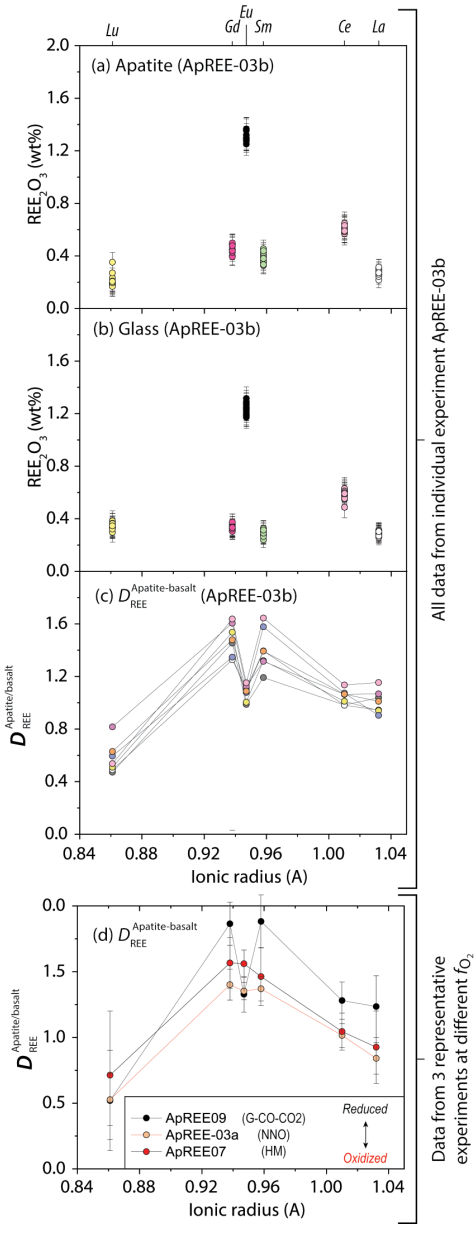

Figure 8. (**a**) Raw EPMA data from experiment ApREE-03b glass analyses, where colors correspond to individual REE_2O_3 (yellow = Lu_2O_3; salmon = Gd_2O_3; black = Eu_2O_3; green = Dy_2O_3; pink = Ce_2O_3; white = La_2O_3). The reported uncertainty (δ) on data points represents the intrinsic error to the EPMA setup and is based on counting statistics. Also note that n = 21 from this experiment. (**b**) Raw EPMA data from apatite from the same experiment ApREE-03b, where REE_2O_3 colors are consistent with previous figure, and n = 8. (**c**) Individual, apatite-glass partition data from experiment ApREE-03b, where color represents a given apatite-glass analytical pair used to make Eu/Eu* calculations (n = 8). (**d**) Apatite/basalt partition coefficients as determined by EPMA from a series of isothermal (1150 °C) experiments equilibrated at different redox buffers. Note the intensity of the negative Eu anomaly (or $Eu/Eu^*)_D$ increases with decreasing [$\log(f_{O_2})$]. HM = hematite-magnetite buffer [$\log(f_{O_2}) = -3.28$], Ni-NiO buffer [$\log(f_{O_2}) = -8.31$], and graphite-CO-CO_2 buffer [$\log(f_{O_2}) = -14.51$]. Error bars reported in **d** as 1σ. (Color online.)

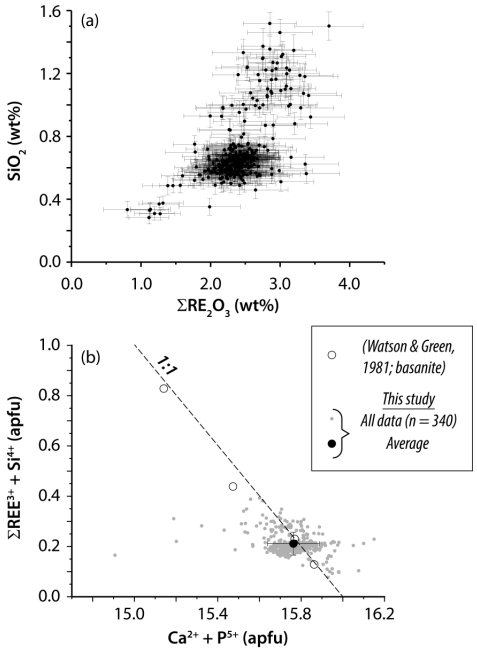

Figure 9. (**a**) ΣREE_2O_3 (assuming CeO_2 and EuO components are negligible, which is consistent with partitioning data, XANES measurements and Eu/Eu* data) vs. SiO_2 content of experimental apatite crystals. Error bars are in 2σ. (**b**) Calculated "REE+Si" vs. "Ca+P" projection in atoms per formula unit (apfu) for all experimental apatite from this study (light gray circles), average from all experiments from this study (with 1δ; solid black circle) and measured compositions from comparable REE partitioning data in mafic apatite-silicate melt experiments by Watson and Green (1981; open circles). Note the dashed 1:1 curve corresponds to the coupled substitution of $REE^{3+} + Si^{4+} = Ca^{2+} + P^{5+}$. Calculations are based on 25 oxygen atoms and assume only Eu^{3+} and Ce^{3+} are present.

(i.e., a 33% decrease in the reported error). Propagating the error for $[(Eu/Eu^*)_D^{\text{lattice strain}}]$ uses all 6 REE elements from our ApREE experiments (La, Ce, Sm, Eu, Gd, and Lu) in both apatite and glass, thus leading to larger error bars when

$$\left(\frac{Eu}{Eu^*}\right)_D^{\sqrt{Sm \times Gd}}$$

and $[(Eu/Eu^*)_D^{\text{lattice strain}}]$ are directly compared. While we see merit in using either method for reporting error—the first involving error propagation, the second involving inter-grain variation in Eu/Eu* without propagating through Sm and Gd)—we have decided to use the former throughout this manuscript.

Comparison of EPMA and LA-ICP-MS results and analytical uncertainty

To assess the quality of the EPMA data from a specific set of experiments, we first take ApREE-06 (buffered at the QFM equilibrium) and observe the statistical variation within the REE measurements (Fig. 7a). If the 34 individual apatite analyses (generally core to rim transects) from 4 apatite crystals are considered we can first note several key observations: (1) all elements show

a normal distribution about the mean (see Fig. 7a); (2) all REEs in the experiment are above detection limits (see $EPMA^{LOD}_{Gd_2O_3}$ and $EPMA^{LOD}_{Smd_2O_3}$ in Fig. 7b); and (3) analytical uncertainty of EPMA analyses ($EPMA_\delta$) is comparable to the intrinsic experimental inter-grain variation (Exp_δ). To emphasize this, Figure 7b shows direct comparison of data from the same experiment (ApREE-06) where we report the analytical uncertainty ($EPMA_\delta$; light error bars) based on spectrometer counting statistics, while inter-grain variation based on analyses from throughout the experiment (Exp_δ; heavy error bars and large circles).

Both EPMA and LA-ICP-MS analyses of experiment ApREE-03b, buffered at Mo-MoO_2 equilibrium (Figs. 7c and 7d) demonstrate that instrumental and inter-grain variation is similar to experiment ApREE-06 and above detection limits. The analytical uncertainty of apatite analyses (see Fig. 7c or $EPMA_\delta$ and $LA\text{-}ICP\text{-}MS_\delta$) is remarkably consistent. Similarly (Fig. 7d), the inter-grain uncertainty (Exp_δ) is also remarkably similar. In other words, the inter-grain variation of REE concentrations in apatite from an experiment does not depend on the analytical technique. The similar inter-grain variation between the two techniques demonstrates the reported error is related to intrinsic experimental variation (i.e., Exp_δ) and as such the calibration curves presented in later Figures (e.g., Figs. 14 and 15) will not be dramatically improved by using techniques with superior counting techniques. Glass analyses (in terms of error) are improved by employment of LA-ICP-MS, whereas apatite analyses are not. Most of the error of the calibrations presented in Equations 12 and 13 (in terms of both $[Eu/Eu^*]_{Sm\text{-}Gd}$ or $[Eu/Eu^*]_{lattice}$) will unlikely be improved greatly by employing other techniques with better counting statistics. (e.g., ion microprobe).

Given that this research is dependent on accurately determining the relative concentration of specific REE—namely La, Ce, Sm, Eu, Gd, and Lu—we present numerous checks in the supplementary material to provide a rigorous evaluation of the data quality (including full wavelength scans of standards, potential overlap calculations/corrections, detection limits, etc.). The greatest check is to directly compare results from EPMA and LA-ICP-MS analyses on common experiments (see Online Materials[1] OM1b and OM2 and Fig. 14). The strong positive correlation between the two techniques provides an internally consistent set of partition coefficients and thus calculated Eu anomalies (Figs. 11c and 11d).

If we take the average detection limit across all EPMA analyses (La = 734 ppm; Ce = 729 ppm; Sm = 663 ppm; Eu = 680 ppm; Gd = 704 ppm; Lu = 1146 ppm) and compare these values directly to LA-ICP-MS from experiment ApREE-07 (La = 0.03 ppm; Ce = 0.03 ppm; Sm = 0.14 ppm; Eu = 0.04 ppm; Gd = 0.15 ppm; Lu = 0.03 ppm; noting all LA-ICP-MS record similar detection limit values), clearly the LA-ICP-MS has lower detection limits. Even so, the measured concentrations reported in Figure 7 are well above these reported detection limits for EPMA. With this in mind, evaluation of the standard deviation (δ) across the two data set shows remarkable similarity (Online Materials[1] Tables OM1a and OM1b; Fig. 7), which demonstrates the two techniques are accurately recording a statistical snapshot of apatite-glass distribution coefficients, and despite having nearly 4 orders of magnitude difference in detection limit, the two sets of data display similar error. In fact in some experiments the LA-ICP-MS methodology records marginally higher error than the EPMA data set despite having a lower LOD (we suggest this relates to the difference in analyte volume across the two techniques). In some cases, techniques with superior counting statistics will improve error in data like that presented in calibration curves presented later (e.g., Figs. 14–15 or calibrations representing Equations 16–17. However in this case, the two techniques record the same error when apatite analyses of single charge are considered, which is strong evidence that the uncertainty is intrinsic to the experimental technique (i.e., reported from multiple analyses from multiple crystals within a common experiment). Thus, the error represents the statistical

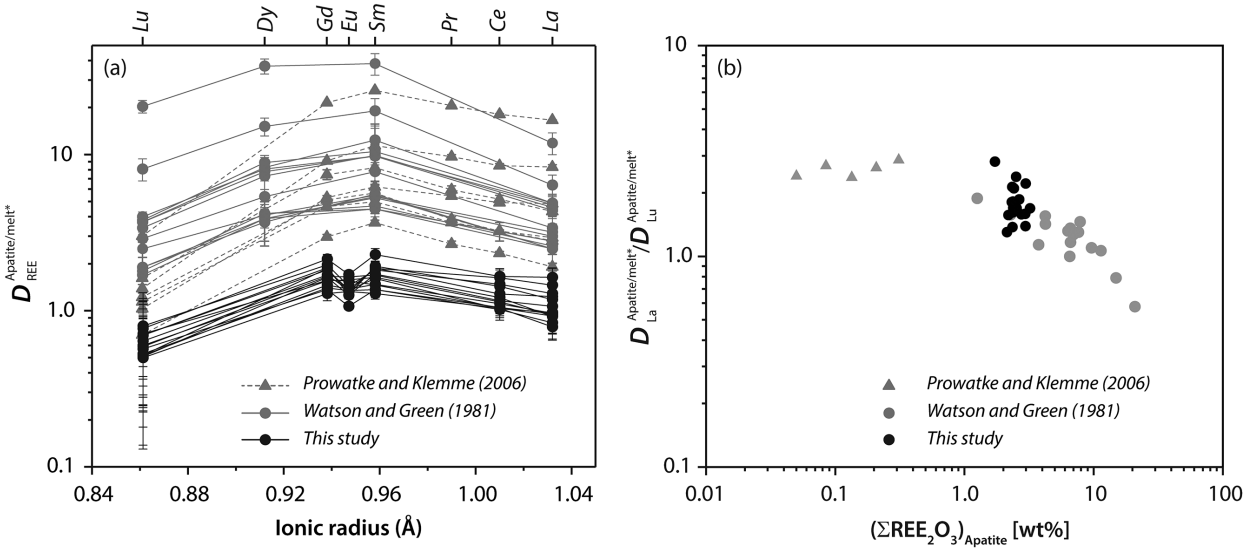

Figure 10. (**a**) Comparison of apatite/silicate melt partition coefficients from this study (ApREE experiments shown by black symbols curves); Watson and Green (1981) (shown by gray circles and solid gray curves); and Prowatke and Klemme (2006) (shown by gray triangles and dashed gray curves). (**b**) Bulk REE content of apatite vs. $D^{apatite/melt}_{La}/D^{apatite/melt}_{Lu}$ (or LREE:HREE), symbols as in **a**. Note: melt* is used because previous studies (Watson and Green 1981; Prowatke and Klemme 2006) include a range of silicate melt types (i.e., not strictly basalt).

variation observed within the population of apatite grains from the experimental technique rather than being related to analytical counting statistics. As a check of this hypothesis, one can compare our results with experimental results by Fleet and Pan (1995) (n = 11 or 12; La-doped = 9.93 ± 0.74, Nd-doped = 12.74 ± 0.54, Gd-doped = 10.36 ± 0.54, Dy-doped = 9.08 ± 0.35), Watson and Green (1981) (n = 7–10; experiment 818 La_2O_3 = 0.29 ± 0.07, Sm_2O_3 = 0.43 ± 0.05, Dy_2O_3 = 0.35 ± 0.06; Lu_2O_3 = 0.19 ± 0.05, experiment 811, La_2O_3 = 0.84 ± 0.10, Sm_2O_3 = 1.47 ± 0.13, Dy_2O_3 = 1.34 ± 0.12, Lu_2O_3 = 0.65 ± 0.10), and Trail et al. 2012 (experiment zfo2_16d: La_2O_3 = 0.232 ± 0.183, Ce_2O_3 = 0.323 ± 0.168, Pr_2O_3 = 0.269 ± 0.155), which are all in the same reported range as those presented here.

Apatite saturation, glass compositions, and application considerations

The apatite saturation results presented here, which include 421 individual glass measurements, show agreement with the Watson (1979) apatite saturation calibration for experiments at 1 bar (Online Materials[1] Fig. OM4). Because the two sets of experiments reproduce similar results they suggest apatite crystallization likely occurred under equilibrium saturation conditions.

The complex multiplicity of potential REE substitution mechanisms in apatite described by Equations 5–8, in conjunction with the compositional range of apatite-saturated magmas, suggests that the activity of other components in the system may influence REE^{3+} and Eu^{2+} partitioning. As described by Equations 5 and 6, the a_{SiO_2} and a_{CaO} in a silicate melt, though difficult to calculate in terms of absolute values without a suitable buffer reaction, all potentially influence the relative partitioning of REE^{3+} and Eu^{2+}. If we take Equation 5 as an example, theory predicts melts of higher silica activity (e.g., rhyolites) will contain apatite of higher $D^{3+}_{\Sigma REE}$ (at a constant REE activity) than silicate melts at lower silicate activity (e.g., basalts). The apatite-melt REE partitioning presented by Watson and Green (1981) helps provide some evidence for the role silica content may play. The more mafic melts presented by Watson and Green (1981) with

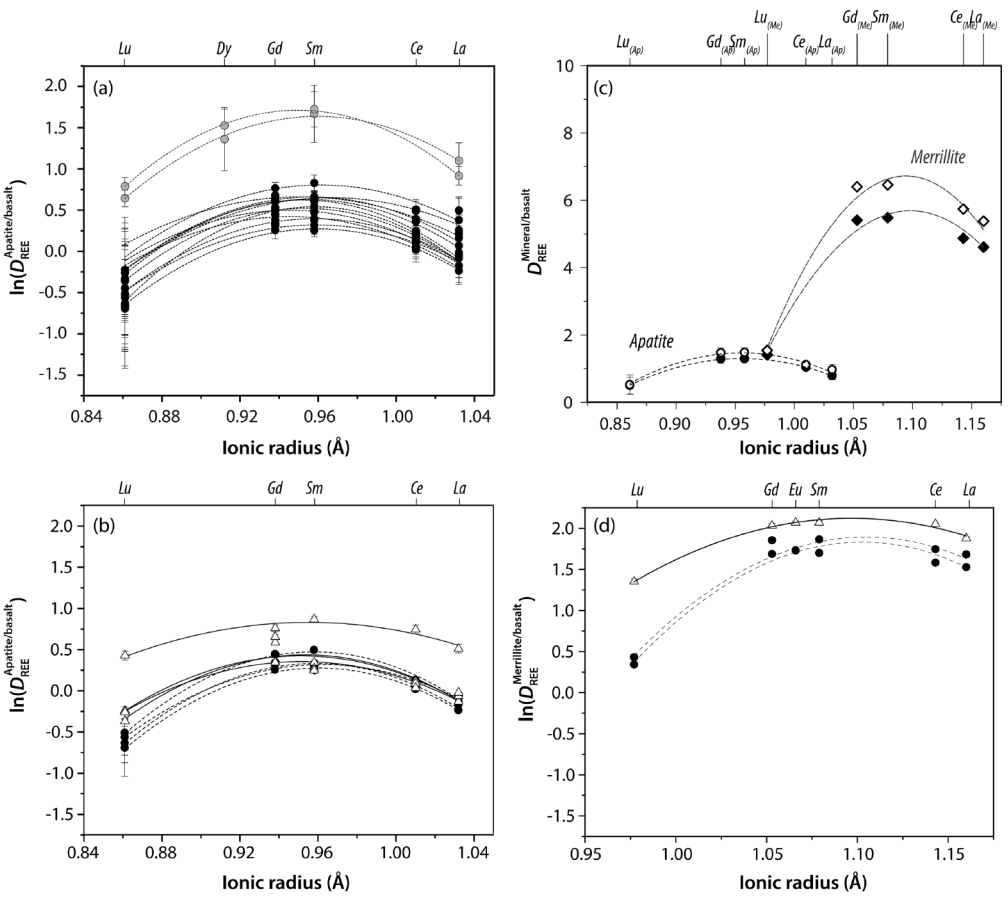

Figure 11. Lattice strain model fits from experiments. (**a**) REE^{3+} partition coefficients with lattice strain models from apatite in all individual experiment data of monovalent $^{[VI]}REE^{3+}$ from this study (black circles), compared with data reported from basanite and tholeiitic andesite by Watson and Green (1981). Note that Ce is included in the model data set because partitioning data indicates no influence from Ce^{4+} over the observed experimental conditions. Error bars reported in 1σ or where absent smaller than symbols. (**b**) REE^{3+} partition coefficients with lattice strain models from apatite four representative experiments using both EPMA (closed circles, dashed lattice strain curve) and LA-ICP-MS (open triangles, solid lattice strain curve) techniques. Note the two techniques record similar partitioning values, similar error and similar lattice strain model topology. (**c**) Lattice strain fits from experiments containing coexisting apatite and merrillite (ApREE-01a and ApREE-04), showing relative REE^{3+} partitioning among the two phosphate phases coexisting with basalt (diamonds correspond to merrillite and circles correspond to apatite). Note data obtained from EPMA, while merrillite ionic radii correspond to 8-coordinated sites of the dominant Ca sites within the mineral with elements in the Figure including La, Ce, Sm, Gd, and Lu (from right to left). (**d**) REE^{3+} partition coefficients with lattice strain models from merrillite based on EPMA (including experiments ApREE-01a and ApREE-04, solid circles, dashed curves) and LA-ICP-MS (experiment ApREE-03a, open triangles, solid curve). Note that though the two techniques show similar topology and error, though direct comparison of data are not possible.

low SiO_2 content (38.4–56.5 wt% SiO_2; basanites, tholeiites, hawaiites, tholeiitic andesites) show notably lower partition coefficients (D_{MREE} = 4.0–6.0) than more silicic melts (56.5–69.7 wt% SiO_2; granites and andesite, where D_{MREE} = 9.0–40.0). When the data from this study and that of Watson and Green (1981) are considered collectively, results indicate melt composition and coupled substitution affect REE partitioning in apatite.

Experimental studies of other accessory phases (e.g., zircon) have shown that mineral solubility is dependent on the alkalinity of a melt. In holocrystalline rocks this is often visualized in terms of the alumina saturation index (ASI) vs. the "Na_2O+K_2O content" (in wt%) from bulk rock analysis. In experimental systems where both glass and mineral compositions can be measured, a slightly different methodology is commonly used, known as the M factor [where M = [Na+K+2·Ca]/[Al·Si] (Watson and Harrison 1983)]. This melt composition control not only plays a role in the solubility of the mineral species but also has the capacity to affect the coordination (and thus partitioning behavior) of REE^{3+} and Eu^{2+}, respectively. It is for this reason, for example, that redox calibrations in zircon require different calibrations (e.g., $[Ce/Ce^*]_D$) depending on the alkalinity of the parent melt (Trail et al. 2012). It is possible then that melts significantly different than those in this study (i.e., peraluminous and peralkaline magmas) likely have different $(Eu/Eu^*)_D$ redox curves from those in Equations 16 and 17, and thus care must be used in applying the results of this study to other experiments and natural samples.

REE site occupancy and partitioning in apatite

A summary of REE partition coefficient data can be found in Online Materials[1] Table OM2 and is shown graphically in Online Materials[1] Fig. OM4 and Figures 9−11. The data presented here can be used to evaluate the REE^{3+} coupled substitution mechanism in apatite within experiments. As outlined in Equation 5–8, several possible substitution mechanisms have been hypothesized. Watson and Green (1981), Fleet and Pan (1994, 1995), and Cherniak (2000) indicate the dominant REE substitution mechanism in fluorapatite involves Si (i.e., Eq. 5). The apatite data from this study (Online Materials[1] Table OM1) and the mafic, REE-doped experiments of Watson and Green (1981) generally show $\Sigma REE^{3+}+Si^{4+}:Ca^{2+}+P^{5+}$ (in apfu) close to the 1:1 coupled substitution, or a strong positive correlation between ΣREE_2O_3 and SiO_2 (Fig. 9). This observation, coupled with the low measured Na content in experimental apatite grains (i.e., generally below detection limit), indicates a single dominant substitution mechanism within experiments.

The REE^{3+} partitioning data for apatite in basalt, here focusing on La, Ce, Sm, Gd, and Lu, all show a general concave down topology when plotted against ionic radii (Figs. 10 and 11). Moreover, direct comparison of EPMA data and LA-ICP-MS data (Fig. 11 and later in Fig. 14) show excellent Onuma topology agreement across the two techniques for both apatite and merrillite. All measured REE^{3+} partition coefficients from apatite straddle unity, with the MREE (Sm, Eu^{3+}, and Gd; D ranging from 1.0–2.0) considered to be marginally compatible, while the LREE and HREE being marginally incompatible (La, Ce^{3+}, Lu; D ranging from 0.5–1.0). Interestingly, these experimental values are similar to REE^{3+} partition coefficient data from lunar apatite grains reported by Jolliff et al. (1993), which record MREE values ~0.4 and LREE and HREE recording slightly lower values (0.12–0.30). This lattice strain topology and compatibility are in agreement with previous experimental work in apatite-saturated melts (Watson and Green 1981; Prowatke and Klemme 2006), all showing the highest compatibility (or the ideal trivalent cation radius in the Onuma diagram) somewhere between Sm and Gd (i.e., MREE). Our observation that all lattice strain calculations from this work indicate that Eu^{3+} is the most proximal REE^{3+} element to the apex of the parabola (i.e., it is the most compatible trivalent element in apatite) suggests that it is theoretically possible to produce a

$$\left(\frac{Eu}{Eu^*}\right)_D^{\sqrt{Sm\times Gd}}$$

slightly >1. This is because Eu^{3+} is slightly more compatible than both Sm and Gd, and thus the square root methodology could result in small positive

$$\left(\frac{Eu}{Eu^*}\right)_D^{\sqrt{Sm\times Gd}}$$

values in highly oxidized systems based on Equation 13. This being the case, partitioning among the $MREE^{3+}$ are so similar that the development of a measurable positive Eu anomaly based on partitioning among Sm^{3+}, Eu^{3+}, and Gd^{3+} is unlikely.

The MREE (Sm, Eu, and Gd) cations show slightly smaller ionic radii than the ideal Ca^{2+} site apatite (be it [XII], [IX], or the simplified [VI] structure used in this study), while Eu^{2+} displays a slightly larger ionic radius than Ca^{2+} in all coordinations relevant to the apatite structure. This could be used to suggest a minor pressure effect on the relative partition coefficient of the two Eu valence species in apatite. This could also be used to explain the marginally higher (i.e., ~half log unit) partition coefficients observed in both the Watson and Green (1981) and Prowatke and Klemme (2006) studies—all equilibrated at pressures between 0.75–2.00 GPa—relative to this study (where experiments were equilibrated at 1 bar). Another plausible explanation for the marginally lower partition coefficients observed in experiments presented here vs. Watson and Green (1981)—the only other experimental study of silicate-apatite systems—is that those experiments were generally conducted at lower temperatures (950–1120 °C). As partition coefficients generally increase with decreasing temperature (see Trail et al. 2012; Watson and Green 1981; Xing et al. 2013) the higher temperature experiments in this study would predict a lower partition coefficient while displaying the same topology. The restricted range of temperatures (1110–1175 °C) and melt compositions (40–50 wt% SiO_2) observed in experiments from this study makes it unsurprising that the topology in REE partitioning data between apatite and basalt are remarkably consistent across all experiments presented here. The similarity in measured partition coefficients justifies the lack of a temperature term in Equation 3, as any temperature effect on REE^{3+} partitioning over the small range in temperature of the present experiments is essentially less than the uncertainties associated with the various analytical techniques.

It is possible to calculate the weighted relative partition coefficient of Eu^{2+} and Eu^{3+} in experiments where both Eu L_3 XANES

$[(Eu^{3+}/\Sigma Eu)_{apatite}]$ and partitioning data

$$\left[\left(\frac{Eu}{Eu^*}\right)_D^{\sqrt{Sm\times Gd}}\right].$$

exist. This represents the first direct evaluation of Eu^{2+} partitioning in apatite, though many previous studies have used Sr^{2+} partitioning data as a proxy for Eu^{2+}. Direct comparison of

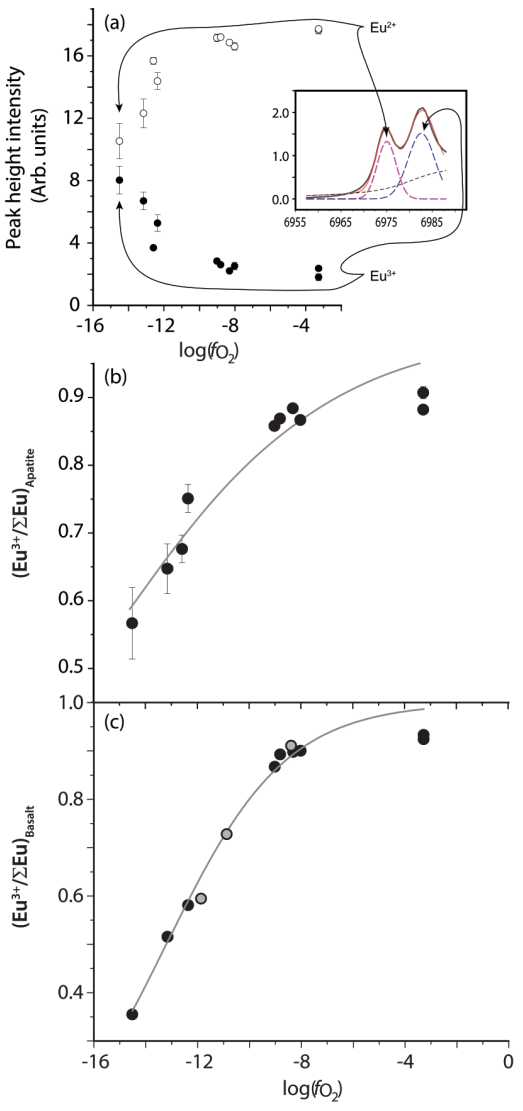

Figure 12. (**a**) Peak height intensity from Eu^{2+} and Eu^{3+} Gaussian curves fit to apatite Eu L_3 XANES data from all experiments used to calculate $Eu^{3+}/\Sigma Eu$. Note the insert represents a single fit to an Eu L_3 XANES spectra from experiment ApREE-09 and is shown for guidance (with dashed purple curve = Eu^{2+} gaussian, dashed blue curve = Eu^{3+} gaussian, dashed black curve = arc tangent, solid red curve = model spectra, and black curve = measured spectrum. (**b**) Valence sigmoid from Eu L_3 XANES data from Table 6 fits to Equation 11 (least squares) from in situ analyses of (**b**) apatite crystals, and (**c**) coexisting glass from individual experiments (black circles) compared to experimental data in basalt presented by Karner et al. (2010) (assuming equilibration at 1130 °C). The Karner et al. (2010) data was not included in the sigmoidal, least squares fit. Error reported in 1σ and where absent is smaller than symbols.

$Eu^{3+}/\Sigma Eu$ XANES speciation curves for basalt and apatite (see Figs. 12b and 12c) converge at $\log(f_{O_2})$ values > –9 (i.e., >QFM), where Eu^{2+} concentrations in both the glass and apatite are small, and the shape of the sigmoid becomes of limited use in terms of defining the redox-related Eu partitioning. To estimate partition coefficients of both Eu valence states, we recommend preferred values (Table 6) based on experiments at $\log(f_{O_2})$ values > –9 (i.e., at f_{O_2} conditions near the locus of the sigmoid inflection). This method yields a combined XANES-EPMA $D_{Eu^{3+}}^{Ap/melt}$ of 1.81 ± 0.26, which is very similar to the average partition coefficient calculated from lattice strain methods applied to all experiments, where $D_{Eu^{3+}}^{Ap/melt}$ is 1.67 ± 0.25. Similarly, the

$$\left(\frac{Eu}{Eu^*}\right)_D^{\sqrt{Sm\times Gd}}$$

method can be used to calculate a $D_{Eu^{3+}}^{Ap/melt}$ of 1.67 ± 0.23 and thus also indicates a value similar to the combined XANES-EPMA $D_{Eu^{3+}}^{Ap/melt}$ of 1.81 ± 0.26. The partition coefficient of divalent Eu calculated from this study indicates Eu^{2+} is less compatible than Eu^{3+} within apatite and records an average $D_{Eu^{3+}}^{Ap/melt}$ of 0.87 ± 0.08 and the $(D_{Eu^{2+}}^{Ap/melt}/D_{Eu^{3+}}^{Ap/melt})$ = 0.48 ± 0.27. The only comparison that can be made is with the apatite-basalt REE partitioning of Watson and Green (1981), whose data can be used in lattice strain calculations to constrain $D_{Eu^{3+}}^{Ap/melt}$, and where $D_{Sr^{2+}}^{Ap/melt}$ can be used to estimate $D_{Eu^{2+}}^{Ap/melt}$. This method results in similar values, where $D_{Eu^{3+}}^{Ap/melt}$ is 5.18 ± 0.35, $D_{Eu^{2+}}^{Ap/melt}$ is 1.35 ± 0.07 and $(D_{Eu^{2+}}^{Ap/melt}/D_{Eu^{3+}}^{Ap/melt})$ = 0.26 ± 0.03. In other words, the techniques described here and re-evaluation of the Watson and Green (1981) data indicate that Eu^{3+} is ~2–4 times more compatible than Eu^{2+} in apatite crystallizing from basalt.

The REE partition coefficients ($D_{REE^{3+}}^{Ap/melt}$) for the strictly trivalent elements (i.e., isovalent cations: La, Sm, Gd, and Lu) are nearly constant over the complete range of experimental f_{O_2} conditions, such that the bulk of the REE appear independent of f_{O_2} (Fig. 13). The Ce partitioning also remains constant over all experimental f_{O_2} suggesting that the Ce^{4+} is highly incompatible in apatite and/or that the oxidation of Ce^{3+} to Ce^{4+} likely exists at higher f_{O_2} conditions than the experimental buffers used. This observation is consistent with previous studies of REE partitioning into the zircon-silicate melt systems (Trail et al. 2012; Burnham and Berry 2012) which demonstrates the $Eu^{2+} \leftrightarrow Eu^{3+}$ transition occurs at much lower f_{O_2} than the Ce^{3+}-Ce^{4+}.

Watson and Green (1981) experimentally demonstrated that at nearly constant melt composition-temperature-pressure-f_{O_2} conditions the REE partitioning behavior remains nearly constant while with H_2O content varies (in terms of wt% and presumably extending to $a_{H_2O}^{silicate\ melt}$). As the Watson and Green (1981) experiments show that H_2O contents generally exceed the content observed in most terrestrial, lunar, and martian basalts, we infer that water activity plays a negligible role in REE partitioning.

Fleet and Pan (1997) speculated that the anion site may also play a role in the coupled substitution of REE^{3+} by virtue of the F^-, Cl^-, and OH^- each affecting the $^{[VII]}Ca(2)$ site (i.e., bond angles and lengths describing the polyhedra) and thus potentially influence REE^{3+} partitioning in apatite. While this may give rise to subtle differences in REE^{3+} partitioning among hydroxyapa-

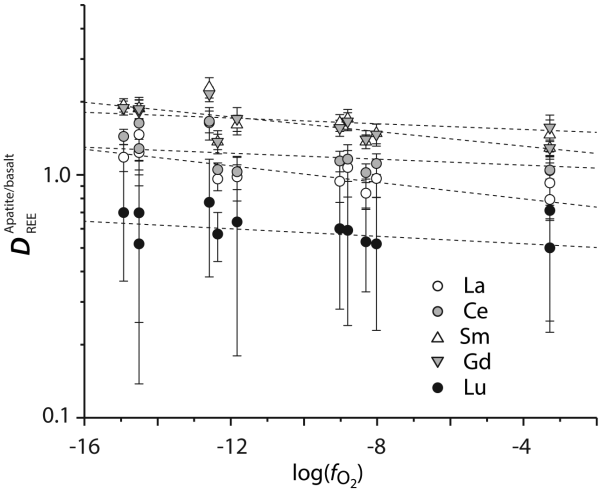

Figure 13. Apatite/melt partition coefficients of isovalent REE^{3+} at various f_{O_2} as determined by EPMA (noting that while Ce is polyvalent, the data indicate only Ce^{3+} is compatible in apatite; see text). Linear regressions for individual elements are represented by sub-horizontal dashed curves and error bars represent 1σ. Note: the near constant partition coefficient observed among the isovalent REE^{3+} demonstrates these elements are unaffected by f_{O_2} over the experimental range. Symbols as indicated; uncertainties are ±1σ.

tite, fluorapatite, and chlorapatite end-members, the dominance of fluorapatite in igneous systems (Piccoli and Candela 2002; Webster and Piccoli 2015) and experiments presented here likely means the anion site control on REE partitioning among magmatic apatite is negligible for the bulk of magmatic redox conditions. The experimental studies into REE solubility among F^- and OH^- apatites by Prowatke and Klemme (2006) also show only subtle differences in REE partitioning, again suggesting the anion site plays little effects REE^{3+} partitioning.

These observations collectively demonstrate the two $(Eu/Eu^*)_D$ calibrations for apatite theoretically laid out in Equations 6 and 7 and defined by calibrations presented in Equations 16 and 17 here are best applied to metaluminous, near-basaltic melts that are similar in composition and pressure to those reported here. In other words, this calibration should not be applied to more silicic systems that are either peralkaline or peraluminous. Further experimentation is needed to accurately extend the working range of the apatite redox sensor to a broader range of magmatic systems, including those of significantly different melt composition (silicic systems, peralkaline and peraluminous systems) and at different pressures (in order to extend use from volcanic to plutonic systems).

Lattice strain calculations and assumptions

The lattice-strain model presented in Equation 11 (Blundy and Wood 1994) has previously been applied to a wide range of phases (e.g., plagioclase, clinopyroxene, garnet, zircon, etc.). Klemme and Dalpé (2003) present calculations made from experimental apatite crystals coexisting with a melt. This calculated Eu^{3+} partition coefficient, which can be determined from a suite of trivalent ions (e.g., REE^{3+}, Y^{3+}, Sc^{3+}, etc.) that substitute on the same structural site(s), can be combined with the measured Eu partition coefficient (which includes both Eu^{2+} and Eu^{3+} components) to determine the intensity of a negative Eu anomaly. Similar methods have been reported for Ce in zircon-melt partitioning studies in the works of Burnham and Berry (2012) and Smythe and Brenan (2016).

The results presented in Online Materials[1] Tables OM1a, OM1b, and OM2 predict REE^{3+} substitution for Ca^{2+} (Eq. 4), so lattice strain calculations assume substitution on the Ca sites within apatite. This being the case, the apatite structure has two Ca sites—here defined as Ca(1) and Ca(2) (Online Materials[1] Fig. OM1). The Ca(1) site can be described as a 9-coordinated, tricapped trigonal prism site where six oxygen atoms form a trigonal prism with bond lengths varying from 2.40–2.46 Å [here modeled on Gd substitution on the Ca(1)-01 and Ca(1)-02 sites (Hughes and Rakovan 2002; Fleet and Pan 1995)]. An additional three O atoms (Ca(1)-03), essentially coplanar with the Ca(1) site, are found at a greater distance (2.81 Å) from the central ion. The Ca(2) site is bound to 6 oxygen atoms with broadly similar ionic radii [Ca(2)-01 = 2.67 Å; Ca(2)-02 = 2.37 Å; Ca(2)-03 = 2.50 Å; Ca(2)-03[d] = 2.35 Å (Hughes and Rakovan 2002; Fleet and Pan

Table 6. $(Eu^{3+}/\Sigma Eu)_{Ap}$ as determined by Eu L_3 XANES apatite-melt at random orientations

Experiment	T (K)	buffer	log (f_{O_2})	n	$(Eu^{3+}/\Sigma Eu)_{Ap}$	(δ)	$(Eu/Eu^*)^{Sm\text{-}Gd}$	(δ)	χ^2	$D_{Eu^{3+}}$	$D_{Eu^{2+}}$
ApREE-01a	1448	NNO	−8.02	6	0.867	0.004	0.94	0.14	0.28	1.35	1.87
ApREE-02	1448	IW	−12.26	12	0.676	0.021	0.73	0.10	0.20	n/a	n/a
ApREE-03a	1423	NNO	−8.31	1	0.884	n/a	0.98	0.09	0.29	1.33	1.53
ApREE-04	1423	HM	−3.28	2	0.907	0.009	1.03	0.11	0.41	1.29	1.83
ApREE-06	1423	QFM	−9.02	3	0.858	0.005	0.99	0.09	0.31	1.57	1.70
ApREE-07	1423	HM	−3.28	3	0.882	0.007	1.03	0.18	0.34	1.52	2.48
ApREE-07	1423	MMO	−12.36	2	0.751	0.021	0.74	0.12	0.28	1.70	0.78
ApREE-09	1423	C-CO-CO_2	−14.51	6	0.567	0.053	0.71	0.15	0.19	2.13	0.89
ApREE-12	1383	NNO	−8.81	2	0.868	0.004	0.98	0.11	0.36	1.59	2.00
ApREE-15X	1383	IW	−13.15	3	0.647	0.037	0.69	0.11	0.24	1.60	0.93
ApREE-2b	1448	IW	−12.59	0.676	0.021	0.72	0.21				
						1.81	0.87				
ApREE-01a	1448	NNO	−8.02	2	0.900	0.003	0.94	0.14	0.28		
ApREE-03a	1423	NNO	−8.31	1	0.898	n/a	0.98	0.09	0.31		
ApREE-04	1423	HM	−3.28	2	0.933	0.000	1.03	0.11	0.42		
ApREE-06	1423	QFM	−9.02	2	0.867	0.002	0.99	0.09	0.33		
ApREE-07	1423	HM	−3.28	2	0.924	0.001	1.03	0.18	0.36		
ApREE-07	1423	MMO	−12.36	2	0.581	0.002	0.74	0.12	0.24		
ApREE-09	1423	C-CO-CO_2	−14.51	5	0.355	0.006	0.71	0.15	0.29		
ApREE-12	1383	NNO	−8.81	2	0.893	0.004	0.98	0.11	0.35		
ApREE-15X	1383	IW	−13.15	2	0.515	0.000	0.69	0.11	0.26		

1995)] and one column anion (X, in experiments generally F). As discussed by Klemme and Dalpé (2003), substitution on both the Ca(1) and Ca(2) sites in apatite is dominated by 6-coordinated structural components, with only minor contributions from the more distal Ca(1)-03 and Ca(2)-F bonds. To make lattice strain calculations and to be consistent with previous calculations made for apatite (Klemme and Dalpé 2003), here the REE^{3+} substitution is based on a simplified sixfold coordination (Online Materials[1] Fig. OM1). As a consequence of this methodology, calculations necessarily assume there is no site preference or change in solubility among the two Ca sites.

While the simplified $^{[VI]}$Ca site can be justified, X-ray diffraction (XRD) unit-cell refinements of high REE-concentration apatite grains (carbonatitic and alkaline magmas) by Hughes et al. (1991 indicates minor site preference for the LREE on the $^{[VII]}$Ca(2) site, no observable site preference for the MREE and, minor preference for the HREE on the $^{[VI+III]}$Ca(1) site. While these site preferences may be important in some systems, the Hughes et al. results indicate no complete exclusion of specific REE on any site, with $REE_{[VII]Ca(2)}/REE_{[VI+III]Ca(1)}$ ranging from 1.8–3.0. As the

$$\left[\left(\frac{Eu}{Eu^*}\right)_D^{\sqrt{Sm\times Gd}}\right]$$

redox calibration is largely dependent on mid-REE, this suggests site preference is highly unlikely to affect Equation 13. The subtle variations in site preference between LREE+HREE and MREE have some capacity to affect the shape of the Onuma projection, and therefore r_0. This could explain the subtle differences in the LREE:MREE ratio seen between the results of this study and the Watson and Green study (1981) vs. that observed in Prowatke and Klemme (2006).

For comparison purposes, lattice calculations $[(Eu/Eu^*)_D^{\text{lattice strain}}]$ made for apatite in Klemme and Dalpé (2003) and in Watson and Green (1981) are included in a complete list of lattice strain calculations from presented in Online Materials[1] Table OM1.

The ionic radius of Eu^{3+} in 6-coordination (0.947 Å) is very similar to the ideal radius calculated from lattice strain averaged from all our apatite-basalt experiments ($r_0 = 0.957 \pm 0.008$ Å) and from data reported by Watson and Green (1981) (0.960 and 0.952 Å for apatite grains reported from mafic systems). This demonstrates the apex of the REE^{3+} parabola or the most compatible REE^{3+} element in apatite is proximal to Eu^{3+}, meaning the most compatible REE in apatite is also the most important variable-valence REE. This is a fortuitous situation in terms of the use of an REE anomaly, as it means the proximity to the apex of the Onuma parabola—when coupled with the relatively incompatible nature of Eu^{2+}—should give rise to the greatest possible resolution in the redox variable element (i.e., the lowest possible analytical uncertainty).

Comparison of $[(Eu/Eu^*)_D^{\text{lattice strain}}]$ and

$$\left[\left(\frac{Eu}{Eu^*}\right)_D^{\sqrt{Sm\times Gd}}\right]$$

is shown in Figures 14 and 15, with the two techniques showing excellent correlation (i.e., plotting very close to the 1:1, with a slope of 0.97 and an intercept of 0.03). As stressed earlier in the discussion, two factors complicate lattice strain models for apatite: (1) Apatite has two distinct cation sites [Ca(1) and Ca(2)] and a complete lattice strain model requires determination of, and projection of, partitioning data for each individual Ca site (a condition not possible to measure via EPMA or LA-ICP-MS); and (2) The various coupled substitution mechanisms for REE partitioning into apatite (see Eqs. 5–8) likely distort the cation site locally (and proportionately for the individual coupled substitution mechanisms) and this likely complicates lattice strain calculations for REE in apatite. Even where the assumptions in the lattice strain model are an oversimplification (e.g., 6-coordination on a single site), the calculated $[\ln(D_0)]$ and r_0 still represent an accurate evaluation of the intensity of the Eu anomaly. The Young's modulus estimates presented in Online Materials[1] Table OM1, by contrast, should be regarded with caution [even though results are consistent with previous methods of Klemme and Dalpé (2003)].

Comparison of the three calibrations. The different analytical techniques and three different Eu valence calibrations presented all show a smooth trend of increasing $(Eu/Eu^*)_D$ or $(Eu^{3+}/\Sigma Eu)_{apatite}$ or $(Eu^{3+}/\Sigma Eu)_{melt}$ with increasing log (f_{O_2}) (see Figs. 12, 14, and 15). The simplest way to envisage the relationship between oxygen fugacity and intensity of $(Eu/Eu^*)_D$ is to directly compare partitioning data among isothermal experiments at different f_{O_2}. This is shown graphically in Figure 8, where 1150 °C experiments at Fe_2O_3-Fe_3O_4 (HM) show no anomaly, Ni-NiO (NNO) shows a small anomaly and C-CO-CO_2 (CCOCO2) shows a pronounced negative Eu anomaly. This change in partitioning behavior follows a sigmoidal relationship in log (f_{O_2})-$(Eu/Eu^*)_D$ or log (f_{O_2})-$(Eu^{3+}/\Sigma Eu)_{apatite}$ space, as would be predicted by Equation 3. By carrying out least squares regressions on experiments using each method (i.e., Eqs. 10, 12, and 13), it is possible to derive redox calibrations for each (shown graphically in Figs. 12 and 15) and these are described in Equations 14–17.

XANES calibration. A total of 9 representative experiments ranging in log(f_{O_2}) from –14.5 to –3.3, or from the graphite-CO-CO_2 buffer to the hematite-magnetite buffer, are used to define the Eu valence sigmoid for both apatite and the coexisting glass. The sigmoid calculated from $(Eu^{3+}/\Sigma Eu)_{apatite}^{XANES}$ data are from individual experiments, presented in Table 6, define the following calibration (Fig. 12):

$$\left(\frac{Eu^{3+}}{\Sigma Eu}\right)_{apatite}^{XANES} = \frac{1}{1+10^{-0.10\pm0.01\times\log(f_{O_2})-1.63\pm0.16}}. \quad (14)$$

The $(Eu^{3+}/\Sigma Eu)_{glass}^{XANES}$, by contrast, reports a calibration shifted slightly to higher f_{O_2} (see Fig. 12):

$$\left(\frac{Eu^{3+}}{\Sigma Eu}\right)_{glass}^{XANES} = \frac{1}{1+10^{-0.15\pm0.01\times\log(f_{O_2})-2.49\pm0.18}}. \quad (15)$$

The minor f_{O_2} shift recorded in calibrations for both apatite and coexisting glass (Fig. 12) is essentially a measure of the differing compatibilities of Eu^{3+} and Eu^{2+} in apatite. As Eu^{3+} is more compatible, the sigmoid shifts to lower f_{O_2} than is observed in the glass. Very similar results have been reported from Eu L_3 XANES spectra from augites in basalt (Karner et al. 2010),

while the inverse relationship is observed between plagioclase and basalt [because Eu^{2+} is the more compatible valence species in plagioclase (Drake 1975)]. It is also possible that some of this offset between the XANES Eu sigmoid between glass and apatite is related to the non-systematic substitution of Eu^{2+} in the different cation sites (i.e., 7- and 9-coordinated polyhedra) when compared directly to Eu^{3+}.

The lattice strain calibration. The lattice strain-based Eu valence calibration or $[(Eu/Eu^*)_D^{\text{lattice strain}}]$ based on results presented in Online Materials[1] Table OM1 and shown graphically in Figure 15b is defined by:

$$\left(\frac{Eu}{Eu^*}\right)_D^{\text{lattice strain}} = \frac{1}{1+10^{-0.20\pm0.03\times\log(f_{O_2})-3.03\pm0.42}} \quad (16)$$

The $\left(\frac{Eu}{Eu^*}\right)_D^{\sqrt{Sm\times Gd}}$ calibration

The Eu valance calibration based on neighboring Sm and Gd or

$$\left[\left(\frac{Eu}{Eu^*}\right)_D^{\sqrt{Sm\times Gd}}\right]$$

records a very similar (as shown in Fig. 15a) trend to the lattice strain calibration and is defined by:

$$\left(\frac{Eu}{Eu^*}\right)_D^{\sqrt{Sm\times Gd}} = \frac{1}{1+10^{-0.15\pm0.03\times\log(f_{O_2})-2.46\pm0.41}}. \quad (17)$$

The "x" in Equation 3, or the coefficient defining the slope of the sigmoid, for all three techniques, 0.10 ± 0.01 from Eu XANES; 0.20 ± 0.03 from $[(Eu/Eu^*)_D^{\text{lattice strain}}]$, and 0.15 ± 0.03 from

$$\left[\left(\frac{Eu}{Eu^*}\right)_D^{\sqrt{Sm\times Gd}}\right],$$

is slightly lower than the theoretical value of 0.25 (Eq. 1). There are many possible explanations for this, but the mostly likely explanation is changing melt composition with changing T and f_{O_2}, with the most reducing experiments [i.e., $\log(f_{O_2}) < -12$] showing a dramatic decrease in FeO* content with the crystallization of schreibersite (see Fig. 16). This change in melt composition and structure likely means the activity coefficients described in Equation 2 are not strictly constant. As discussed earlier, oxide solid-state buffers can also influence glass/melt composition within experiments, which may also subtly influence activity coefficients across different experiments. This is the most likely cause for the difference between measured and theoretical coefficients for the sigmoid, but we note that natural basalts crystallizing at low f_{O_2} (e.g., lunar basalts) can also exhibit native iron (metal) and also likely undergo dramatic changes in melt composition during fractionation.

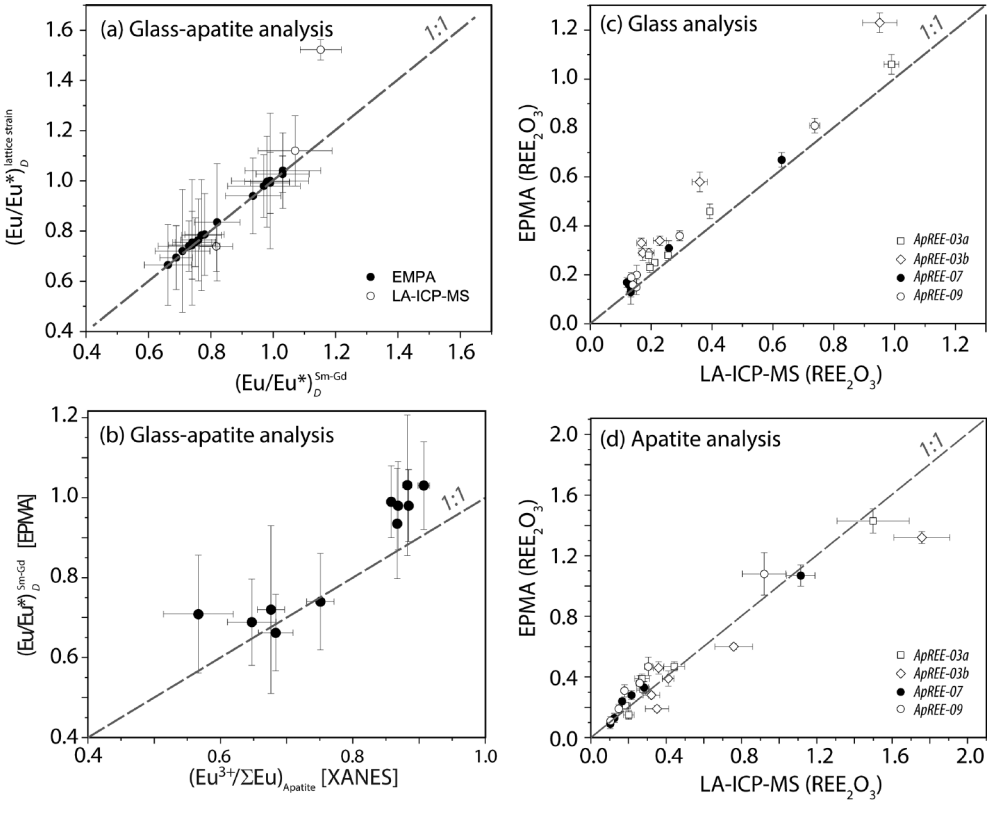

FIGURE 14. (**a**) Comparison of (Eu/Eu*) in apatite as determined by lattice strain [i.e., $(Eu/Eu^*)_D^{\text{lattice strain}}$] vs. (Eu/Eu*) as determined by the concentration of neighboring REEs Sm-Gd [i.e., $(Eu/Eu^*)_D^{\text{Sm-Gd}}$]. Open symbols represent LA-ICP-MS data and closed symbols represent EPMA data. (**b**) Comparison of (Eu/Eu*) as determined by neighboring REEs Sm-Gd vs. Eu/ΣEu determined from XANES for experiments where both analytical techniques have been applied. (**c**) Comparison of REE concentration reported in REE_2O_3 (including La_2O_3, Ce_2O_3, Sm_2O_3, Eu_2O_3, Gd_2O_3, Lu_2O_3) analyses from glass as determined by LA-ICP-MS and EPMA. (**d**) Comparison of REE_2O_3 analyses (same elemental oxides as listed in Fig. 15c) from apatite grains within an individual experiment as determined by LA-ICP-MS and EPMA. Error bars represent 1σ. Note: dashed curves in graphs (**a** and **d**) represent 1:1 curve across the two analytical techniques being compared (i.e., EPMA vs. LA-ICP-MS, etc.).

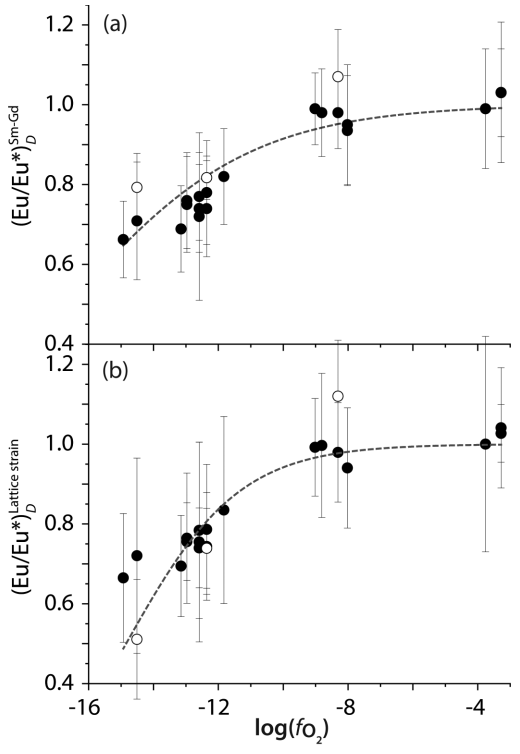

Figure 15. Eu valence speciation curves for apatite-basalt defined by experiments and obtained through least squares regression to data from Online Materials[1] Table S2. (**a**) $(Eu/Eu^*)_D^{Sm\text{-}Gd}$ calibration curve as determined by EPMA, error in 1σ. (**b**) $(Eu/Eu^*)_D^{lattice\ strain}$ calibration curve as determined by EPMA, error in 1δ. Closed circles in both figures represent EPMA data and open circles correspond to LA-ICP-MS data.

Comments on merrillite REE partitioning

Several experiments permit an evaluation of the relative partitioning of REE^{3+} and Eu^{2+} valence species between apatite-merrillite-silicate melt at oxidized conditions (ApREE-01a and ApREE-04). The merrillite results presented here should only be considered a guide to partitioning, as further experimentation is required to confirm partitioning over a full range of f_{O_2} The Onuma diagram from LA-ICP-MS and EPMA techniques are in excellent agreement and the topology of the Onuma diagram for both phases are similar, though the LREE:HREE (as measured by La/Lu) tends to be lower in apatite (1.79 ± 0.38) than in merrillite (3.05 ± 0.57). As shown in Figures 11c and 17a, the $D_{REE^{3+}}$ are ~2.9 (Lu) to ~5.7 (La) times more compatible, approximately half an order of magnitude, in merrillite than in apatite (see Online Materials[1] OM2). This similarity in partition coefficients and topology suggests the that two phases are unlikely to fractionate REE^{3+} sufficiently to dramatically change parameters used to constrain the intensity of an Eu anomaly [i.e., $(Eu/Eu^*)_D$; parameters like $\sqrt{Sm \times Gd}$ or the topology of the lattice strain parabola.

Comparison of $(Eu/Eu^*)_D^{Sm\text{-}Gd}$ for merrillite and apatite (see Fig. 17) demonstrates that the two phases show a positive correlation among Eu valence species. As shown in Figures 10a and 10b, experiments at the hematite-magnetite buffer [log(f_{O_2}) = –3.28] show a mildly positive $(Eu/Eu^*)_D^{Sm\text{-}Gd}$ in both merrillite (1.04 ± 0.02) and apatite (1.03 ± 0.11), whereas at the Ni-NiO buffer [log(f_{O_2}) = –8.02] both phases show the development of a small negative anomaly, with $(Eu/Eu^*)_D^{Sm\text{-}Gd}$ merrillite (0.88 ± 0.02) and apatite (0.94 ± 0.14). From this limited data set it can be hypothesized that Eu^{2+} is slightly more incompatible in merrillite than in apatite, leading to the merrillite recording slightly larger negative Eu anomalies than apatite. This being the case, the relative difference in compatibility between REE^{3+} and Eu^{2+} is sufficiently small that neither phase (merrillite or apatite) is likely to significantly influence oxygen fugacity estimates made from the other phase based on either $(Eu/Eu^*)_D^{Sm\text{-}Gd}$ or $(Eu/Eu^*)_D^{lattice\ strain}$. This is true whether both phases co-crystallize or where phase saturation occurs at different times/temperatures in the liquid line of decent (i.e., saturation of one phase occurs earlier than the other).

Application to natural apatite. Existing REE valence calibrations in minerals, namely Ce/Ce*-in-zircon (Trail et al. 2012; Burnham and Berry 2012; Smythe and Brenan 2016), can be applied to "out of context" grains under specific circumstances, largely because independent thermometers for the mineral exist (e.g., Ti-in-zircon or zircon saturation models). This is because Ce^{4+}/Ce^{3+} is not considered to be strongly fractionated from neighboring LREE by crystallization of additional phases during magmatic evolution. The same scenario is not true of magmatic apatite, and there are two major concerns regarding application of Equations 16 and 17: fractionation of Eu^{3+}/Eu^{2+} during crystal-melt evolution can be influenced by the crystallization of phase(s) that preferentially partition one of the Eu valence species, thus giving rise to spurious estimates of the Eu/Eu*, and basaltic melts can have an intrinsic Eu^{3+}/Eu^{2+} derived from the composition of the melt source.

Previous f_{O_2}-temperature experimental studies, combined with this study into basaltic systems, demonstrate that augite, diopside, and apatite (and on the basis of crystal structures/compositions, presumably olivine and spinel) all show partition coefficients where $D_{Eu^{2+}}^{mineral/melt} < D_{Eu^{3+}}^{mineral/melt}$, and where $D_{Eu^{3+}}^{mineral/melt}$ are approximately at or below unity (see Fig. 17). Calculations based on natural systems (e.g., Schnetzler and Philpotts 1970; Jolliff et al. 1993, 2006) and experimental studies by Drake (1972) and Drake and Weill (1975), demonstrate that the partition coefficient of Eu^{2+} in plagioclase is significantly higher than for other REE^{3+}. The experiments of Drake (1972) equilibrated at 1290–1300 °C, for example, show $D_{Eu^{2+}}^{plag/basalt} = 1.65$, while $D_{Eu^{3+}}^{plag/basalt} = 0.045$ (at temperatures comparable to this study). This partitioning behavior, particularly in melts existing at an f_{O_2} that approximates the inflection point of the $Eu^{2+} \leftrightarrow Eu^{3+}$ sigmoid (i.e., existing at mixed valence state), has the capacity to significantly fractionate Eu from neighboring Sm and Gd (thus influencing estimates of f_{O_2} made from revised Equations 12 and 13; i.e., where melt composition cannot be analyzed). Moreover, these studies (Drake 1972; Drake and Weill 1975) indicate that while Eu^{3+}, Sm, and Gd partitioning appear to be insensitive to temperature variations (i.e., the slope approaches zero in $1/T - \ln D_{Eu^{3+}}^{plag/basalt}$ space; see Fig. 18), the partitioning of Eu^{2+} appears to show a notable temperature effect. The work of Drake (1972, 1975) and Drake and Weill (1975) show increasing compatibility with decreasing temperature (as is the case for most trace elements)—but this temperature effect is also accompanied by a change in plagioclase composition (from anorthitic to albitic compositions with decreasing temperature). The net result of

decreasing temperature and changing plagioclase composition is that a melt develops an increasing negative Eu anomaly with progressive plagioclase crystallization. Given the control of bulk composition on the liquid line of descent—particularly the temperatures, composition, and quantity of plagioclase and apatite crystallization—each basaltic system likely needs to be considered individually (i.e., there is no unique solution that can be broadly applied among basalts). If apatite and plagioclase crystallize at similar conditions, or the temperature-composition interval for each phase can be calculated, then the reciprocal relationship among the Eu/Eu* (i.e., the intensity of the negative anomaly in apatite and positive anomaly in coexisting plagioclase) should converge on a commonly calculated f_{O_2} and could be used to evaluate f_{O_2} equilibria among coexisting phases. See Online Materials[1] Appendix OM4 for a simplified example of calculating the effect of plagioclase fractionation on

$$\left[\left(\frac{\mathrm{Eu}}{\mathrm{Eu}^*}\right)_D^{\sqrt{\mathrm{Sm}\times\mathrm{Gd}}}\right].$$

The second major concern regarding Equations 12 and 13 (where melt composition cannot be measured), is whether the parent melt from which apatite saturates has an intrinsic Eu anomaly inherited from the source material. Where global MORB (N-MORB or E-MORB) appear to show no negative Eu anomaly, this likely relates to the lack of plagioclase in the mantle source region. This observation is not universally true of all basaltic melt sources. Lunar basalts, for example, all record a pronounced negative Eu anomaly thought to be related to the development of the lunar highlands (e.g., plagioclase fractionation from the lunar magma ocean). In cases where there is an intrinsic anomaly, it is possible to calculate the effect of an inherited negative europium anomaly (Eu/Eu*) if the melt Eu^{2+}:Eu^{3+} is fixed at a given f_{O_2} (i.e., defined by XANES data) and partitioning is concentration independent and constant. Examples for

$$\left(\frac{\mathrm{Eu}}{\mathrm{Eu}^*}\right)_D^{\sqrt{\mathrm{Sm}\times\mathrm{Gd}}}$$

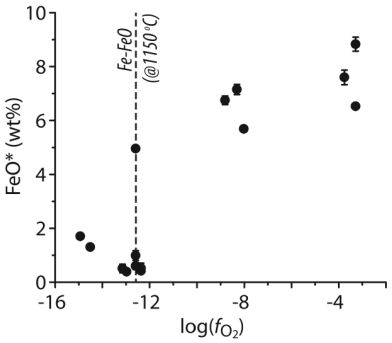

Figure 16. Average FeO* from ApREE experimental glasses vs. log(f_{O_2}). Note that most experiments at very reducing conditions [i.e., log(f_{O_2}) < –12] report low FeO* and generally show the presence of schreibersite.

Table 7. (Eu^{3+}/ΣEu)Ap as determined by Eu L3 XANES on oriented apatite

Scan no.	Orientation (relative to north)	Eu^{2+} [$\varphi_{(6975.5\ eV)}$]	σ	Eu^{3+} [$\varphi_{(6983.3\ eV)}$]	σ	arctan	χ^2	reduced χ^2	R-factor	Eu^{3+}/ΣEu	% valence change (Δ°)
					ApREE-12						
ApREE_12_ap4_0	0°	4.960	0.152	12.588	0.109	1.034	0.285	0.002	0.001	0.717	
ApREE_12_ap4_60	60°	4.977	0.154	13.467	0.120	1.013	0.364	0.002	0.002	0.730	7.848
ApREE_12_ap4_120	120°	5.924	0.160	12.184	0.114	1.029	0.319	0.002	0.001	0.673	
ApREE_12_ap3_0	0°	5.815	0.161	12.398	0.117	1.032	0.333	0.002	0.001	0.681	
ApREE_12_ap3_60	60°	5.606	0.154	12.987	0.118	1.001	0.358	0.003	0.002	0.698	2.989
ApREE_12_ap3_120	120°	5.715	0.156	12.012	0.109	1.041	0.280	0.002	0.001	0.678	
ApREE_12_ap2_0	0°	6.072	0.160	11.377	0.103	1.082	0.240	0.002	0.001	0.652	
ApREE_12_ap2_60	60°	5.756	0.162	12.692	0.114	1.074	0.308	0.002	0.001	0.688	5.229
ApREE_12_ap2_120	120°	5.823	0.159	11.838	0.109	1.039	0.279	0.002	0.001	0.670	
ApREE_12_ap1_0	0°	5.956	0.168	11.708	0.112	1.072	0.284	0.002	0.001	0.663	
ApREE_12_ap1_60	60°	5.851	0.181	12.667	0.120	1.086	0.329	0.002	0.002	0.684	5.406
ApREE_12_ap1_120	120°	6.120	0.165	11.220	0.107	1.072	0.254	0.002	0.001	0.647	
Average		5.722	0.161	12.383	0.114	1.044	0.311	0.002	0.001	0.684	
Standard deviation		0.337	0.009	0.711	0.005	0.031	0.039	0.000	0.000	0.024	
					ApREE-02						
ApREE_2_ap1_0	0°	5.154	0.138	12.002	0.107	1.035	0.239	0.002	0.001	0.700	
ApREE_2_ap1_60	60°	4.679	0.147	12.363	0.101	1.059	0.221	0.002	0.001	0.725	7.215
ApREE_2_ap1_120	120°	5.486	0.145	11.296	0.093	1.089	0.182	0.001	0.001	0.673	
ApREE_2_ap2_0	0°	5.723	0.157	11.785	0.107	1.040	0.251	0.002	0.001	0.673	
ApREE_2_ap2_60	60°	5.529	0.148	11.542	0.097	1.078	0.207	0.002	0.001	0.676	1.366
ApREE_2_ap2_120	120°	5.620	0.148	11.251	0.095	1.063	0.197	0.001	0.001	0.667	
ApREE_2_ap3_0	0°	5.282	0.143	11.758	0.095	1.071	0.198	0.001	0.001	0.690	
ApREE_2_ap3_60	60°	5.690	0.149	11.500	0.098	1.071	0.206	0.002	0.001	0.669	5.803
ApREE_2_ap3_120	120°	5.721	0.155	10.624	0.101	1.144	0.171	0.001	0.001	0.650	
ApREE_2_ap4_0	0°	5.934	0.155	11.157	0.097	1.106	0.195	0.001	0.001	0.653	
ApREE_2_ap4_60	60°	5.580	0.150	11.492	0.097	1.085	0.201	0.001	0.001	0.673	3.023
ApREE_2_ap4_120	120°	5.370	0.148	10.761	0.097	1.112	0.163	0.001	0.001	0.667	
Average		5.481	0.149	11.461	0.099	1.079	0.203	0.001	0.001	0.676	
Standard deviation		0.330	0.005	0.492	0.004	0.031	0.025	0.000	0.000	0.021	
Average orientation-dependent percentage variation in Eu^{3+}/ΣEu											4.860
Standard deviation											2.232

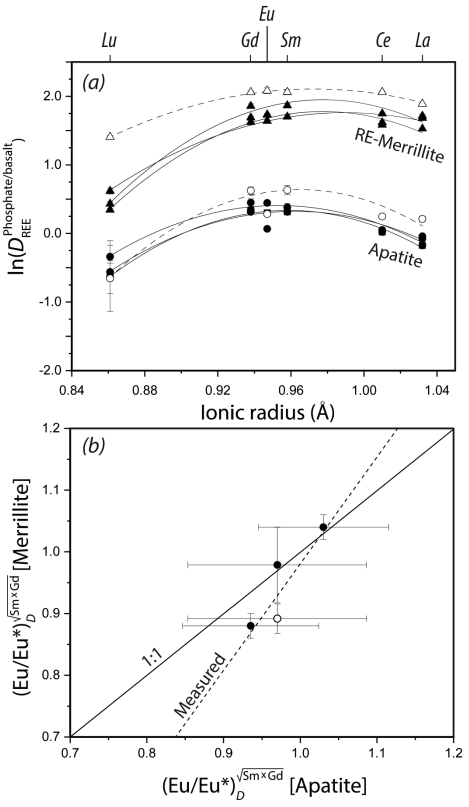

Figure 17. Measured REE partition coefficients in experiments containing coexisting merrillite and apatite within syn-KREEP 15386-01a basalt. (**a**) Data from experiments ApREE-01a, ApREE-03a, ApREE-04 from oxidized experiments (i.e., Fe_2O_3-Fe_3O_4 or Ni-NiO buffers), where triangles correspond to RE-merrillite analyses, circles correspond to apatite analyses, open symbols represent LA-ICP-MS analyses and closed symbols represent electron microprobe analyses. Error is in 1σ. Note that ionic radii in **a** corresponds to a theoretical 6-coordinated site (as in Fig. 2) and is not an accurate projection for merrillite but is used such that the two different crystal structures can be directly comparted via projection. The relative topography of the Onuma diagram and depth of the Eu anomaly in **a** can, however, be used as a guide to the relative partitioning behavior between merrillite-basalt and apatite-basalt. (**b**) Direct comparison of $(Eu/Eu^*)_D^{Sm\text{-}Gd}$ or intensity of the negative Eu anomaly in coexisting merrillite and apatite for the same set of experiments (i.e., ApREE-01a, ApREE-03a, and ApREE-04) with direct comparison to 1:1 curve. As in previous figure open symbols correspond to LA-ICP-MS analyses and closed symbols correspond to electron microprobe analyses.

corrected for equilibrium fractionation of plagioclase and for inherited Eu anomalies are presented in Online Materials[1] Table OM2. While these calculations involve simplifications, demonstrate methodologies that can be used to make Eu valence corrections.

Clearly the "best-case" scenario for all valence calibrations presented involves situations where partitioning pairs (i.e., apatite-melt) can be calculated from melt inclusions hosted in apatite, or where apatite is found within glass, such that the two phases share a near contemporaneous temperature and chemical history. Whole rock analysis may be used to calculate REE concentrations within a melt, but the relative timing of phase crystallization (which can effectively fractionate the REE) will be crucial to interpreting any

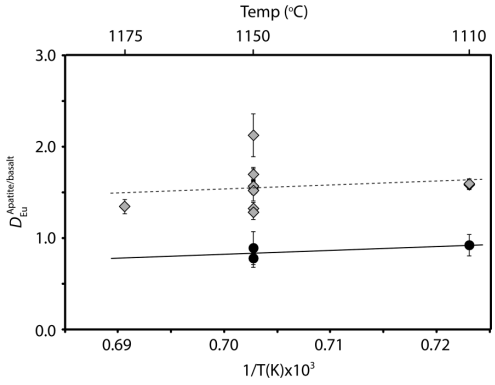

Figure 18. Linear regressions to Eu partition coefficients for Eu^{3+} (gray diamonds) and Eu^{2+} (black circles; preferred values) determined from experiments where both EPMA and Eu L_3 XANES data has been obtained.

calculated REE abundance. Similarly, if the melt composition changes significantly during fractional crystallization and REE are fractionated during crystallization of an accessory phase, bulk analysis can lead to spurious calculations.

Implications

This experimental study demonstrates that partitioning of Eu valence species into apatite can be used as an effective oxygen fugacity sensor. The REE content of apatite, like other phases that may potentially crystallize from metaluminous melts (e.g., zircon, pyroxene, etc.), can be used to determine redox conditions [$\log(f_{O_2})$] in basaltic systems over a 1110–1175 °C range. Application of this calibration is best carried out in systems where coexisting apatite and glass are present (e.g., melt inclusions in volcanic apatite phenocrysts or where glass-apatite are immediately adjacent); under such circumstances no corrections for fractionation (e.g., plagioclase crystallization) or inherited anomalies need be considered. Numerous studies into the various meteorite and Apollo collections, which demonstrate apatite abundance within a range of mafic rocks, suggest that the calibration has broad application and can be used to evaluate the oxidation state of numerous terrestrial bodies.

Acknowledgments

The authors thank Daniel Harlov and Justin Filiberto for organizing this special volume in memory of our friend and colleague Jim Webster. N.D.T. enjoyed numerous discussions with Jim during the development of this study, and we hope the paper promotes further experimental work on apatite, something we believe Jim would appreciate and approve of. The authors thank Adrian Fiege for assistance with Virtual WDS software and general awesomeness, Antony Burnham for assistance with Eu valence fityk code, and John Hughes and George Harlow for providing apatite structural models. The various reviewers of this paper are also thanked for improving on earlier versions.

Funding

This research was partially funded under the NASA Astrobiology Institute grant no. NNA09DA80A to RPI. Portions of this work were performed at GeoSoilEnviroCARS (The University of Chicago, Sector 13), Advanced Photon Source (APS), Argonne National Laboratory. GeoSoilEnviroCARS is supported by the National Science Foundation, Earth Sciences (EAR-1634415) and Department of Energy-GeoSciences (DE-FG02-94ER14466). This research used resources of the Advanced Photon Source, a U.S. Department of Energy (DOE) Office of Science User Facility operated for the DOE Office of Science by Argonne National Laboratory under Contract No. DE-AC02-06CH11357. This work was partially supported by EAR-1751903.

References cited

Barbarand, J. and Pagel, M. (2001) Cathodoluminescence study of apatite crystals. American Mineralogist, 86, 473–484, https://doi.org/10.2138/am-2001-0411.

Berry, A.J. and O'Neill, H.St.C. (2004) A XANES determination of the oxidation state of chromium in silicate glasses. American Mineralogist, 89, 790–798, https://doi.org/10.2138/am-2004-5-613.

Blundy, J. and Wood, B. (1994) Prediction of crystal-melt partition coefficients from elastic moduli. Nature, 372, 452–454, https://doi.org/10.1038/372452a0.

Boyce, J.W., Liu, Y., Rossman, G.R., Guan, Y., Eiler, J.M., Stolper, E.M., and Taylor, L.A. (2010) Lunar apatite with terrestrial volatile abundances. Nature, 466, 466–469, https://doi.org/10.1038/nature09274.

Brice, J.C. (1975) Some thermodynamic aspects of the growth of strained crystals. Journal of Crystal Growth, 28, 249–253, https://doi.org/10.1016/0022-0248(75)90241-9.

Brounce, M., Boyce, J., McCubbin, F.M., Humphreys, J., Reppart, J., Stolper, E., and Eiler, J. (2019) The oxidation state of sulfur in lunar apatite. American Mineralogist, 104, 307–312, https://doi.org/10.2138/am-2019-6804.

Burnham, A.D. and Berry, A.J. (2012) An experimental study of trace element partitioning between zircon and melt as a function of oxygen fugacity. Geochimica et Cosmochimica Acta, 95, 196–212, https://doi.org/10.1016/j.gca.2012.07.034.

——— (2014) The effect of oxygen fugacity, melt composition, temperature and pressure on the oxidation state of cerium in silicate melts. Chemical Geology, 366, 52–60, https://doi.org/10.1016/j.chemgeo.2013.12.015.

Burnham, A.D., Berry, A.J., Halse, H.R., Schofield, P.F., Cibin, G., and Mosselmans, J.F.W. (2015) The oxidation state of europium in silicate melts as a function of oxygen fugacity, composition and temperature. Chemical Geology, 411, 248–259, https://doi.org/10.1016/j.chemgeo.2015.07.002.

Cherniak, D.J. (2000) Rare earth element diffusion in apatite. Geochimica et Cosmochimica Acta, 64, 3871–3885, https://doi.org/10.1016/S0016-7037(00)00467-1.

Cicconi, M.R., Giuli, G., Paris, E., Ertel-Ingrisch, W., Ulmer, P., and Dingwell, D.B. (2012) Europium oxidation state and local structure in silicate glasses. American Mineralogist, 97, 918–929, https://doi.org/10.2138/am.2012.4041.

Delano, J.W. (1990) Experimental constraints on the oxidation state of the lunar mantle. Lunar and Planetary Science Conference XXI, 278–279. Lunar and Planetary Institution, Houston.

Drake, M.J. (1972) The distribution of major and trace elements between plagioclase feldspar and magmatic silicate liquid: an experimental study, 191 p. Ph.D. thesis, University of Oregon.

——— (1975) The oxidation state of europium as an indicator of oxygen fugacity. Geochimica et Cosmochimica Acta, 39, 55–64, https://doi.org/10.1016/0016-7037(75)90184-2.

Drake, M.J. and Weill, D.F. (1975) Partition of Sr, Ba, Ca, Y, Eu^{2+}, Eu^{3+}, and other REE between plagioclase feldspar and magmatic liquid: An experimental study. Geochimica et Cosmochimica Acta, 39, 689–712, https://doi.org/10.1016/0016-7037(75)90011-3.

Elderfield, H., Hawkesworth, C.J., Greaves, M.J., and Calvert, S.E. (1981) Rare earth element geochemistry of oceanic ferromanganese nodules and associated sediments. Geochimica et Cosmochimica Acta, 45, 513–528, https://doi.org/10.1016/0016-7037(81)90184-8.

Fleet, M.E. and Pan, Y. (1994) Site preference of Nd in fluorapatite [$Ca_{10}(PO_4)_6F_2$]. Journal of Solid State Chemistry, 112, 78–81, https://doi.org/10.1006/jssc.1994.1268.

——— (1995) Site preference of rare earth elements in fluorapatite. American Mineralogist, 80, 329–335, https://doi.org/10.2138/am-1995-3-414.

——— (1997) Rare earth elements in apatite: Uptake from H_2O-bearing phosphate-fluoride melts and the role of volatile components. Geochimica et Cosmochimica Acta, 61, 4745–4760, https://doi.org/10.1016/S0016-7037(97)00292-5

Goles, G., Randle, K., Osawa, M., Schmitt, R.A., Wakita, H., Ehmann, W.D., and Morgan, J.W. (1970) Elemental abundances by instrumental activation analyses in chips from 27 lunar rocks. Proceedings of the Apollo 11 Lunar Science Conference.2, 1165–1176.

Green, T.H. and Watson, E.B. (1982) Crystallization of apatite in natural magmas under high pressure, hydrous conditions, with particular reference to "orogenic" rock series. Contributions to Mineralogy and Petrology, 79, 96–105, https://doi.org/10.1007/BF00376966.

Greenwood, J.P., Itoh, S., Sakamoto, N., Warren, P., Taylor, L., and Yurimoto, H. (2011) Hydrogen isotope ratios in lunar rocks indicate delivery of cometary water to the Moon. Nature Geoscience, 4, 79–82, https://doi.org/10.1038/ngeo1050.

Grutzeck, M., Kridelbaugh, S., and Weill, D. (1974) The distribution of Sr and REE between diopside and silicate liquid. Geophysical Research Letters, 1, 273–275, https://doi.org/10.1029/GL001i006p00273.

Helmke, P.A., Blanchard, D.P., Haskin, L.A., Telander, K., Weiss, C., and Jacobs, J.W. (1973) Major and trace elements in igneous rocks from Apollo 15. The Moon, 8, 129–148, https://doi.org/10.1007/BF00562754.

Henderson, C.E. (2011) Protocols and pitfalls of electron microprobe analysis of apatite, 68 p. Masters thesis, University of Michigan.

Herd, C.D.K. (2008) Basalts as probes of planetary interior redox state. Reviews in Mineralogy and Geochemistry, 68, 527–553, https://doi.org/10.2138/rmg.2008.68.19.

Hoskin, P.W.O. and Schaltegger, U. (2003) The composition of zircon and igneous and metamorphic petrogenesis. Reviews in Mineralogy and Geochemistry, 53, 27–62. https://doi.org/10.2113/0530027.

Hubbard, N.J., Gast, P.W., Rhodes, J.M., Bansal, B.M., and Wiesmann, H. (1972) Nonmare basalts: Part II. Proceedings of the Third Lunar Science Conference. 2, 1161–1179.

Hughes, J.M., Cameron, M., and Mariano, A.N. (1991) Rare-earth-element ordering and structural variations in natural rare-earth-bearing apatites. American Mineralogist, 76, 1165–1173.

Hughes, J.M., Jolliff, B.L., and Gunter, M.E. (2006) The atomic arrangement of merrillite from the Fra Mauro Formation, Apollo 14 lunar mission: The first structure of merrillite from the Moon. American Mineralogist, 91, 1547–1552, https://doi.org/10.2138/am.2006.2021.

Hughes, J.M. and Rakovan, J. (2002) The crystal structure of apatite, $Ca_5(PO_4)_3(F,OH,Cl)$. Reviews in Mineralogy and Geochemistry, 48, 1–12, https://doi.org/10.2138/rmg.2002.48.1.

——— (2015) Structurally robust, chemically diverse: apatite and apatite supergroup minerals. Elements, 11, 165–170, https://doi.org/10.2113/gselements.11.3.165.

Jolliff, B.L., Haskin, L.A., Colson, R.O., and Wadhwa, M. (1993) Partitioning in REE-saturating minerals: Theory, experiment, and modelling of whitlockite, apatite, and evolution of lunar residual magmas. Geochimica et Cosmochimica Acta, 57, 4069–4094, https://doi.org/10.1016/0016-7037(93)90354-Y.

Jolliff, B.L., Hughes, J.M., Freeman, J.J., and Zeigler, R.A. (2006) Crystal chemistry of lunar merrillite and comparison to other meteoritic and planetary suites of whitlockite and merrillite. American Mineralogist, 91, 1583–1595, https://doi.org/10.2138/am.2006.2185.

Karner, J.M., Papike, J.J., Sutton, S.R., Burger, P.V., Shearer, C.K., Le, L., Newville, M., and Choi, Y. (2010) Partitioning of Eu between augite and a highly spiked martian basalt composition as a function of oxygen fugacity (IW-1 to QFM): Determination of Eu^{2+}/Eu^{3+} ratios by XANES. American Mineralogist, 95, 410–413, https://doi.org/10.2138/am.2010.3394.

Kato, Y., Kano, T., and Kunugiza, K. (2002) Negative Ce anomaly in the Indian Banded Iron Formations: Evidence for the emergence of oxygenated deep-sea at ~2.9–2.7 Ga. Resource Geology, 52, 101–110, https://doi.org/10.1111/j.1751-3928.2002.tb00123.x.

Klemme, S. and Dalpé, C. (2003) Trace-element partitioning between apatite and carbonatite melt. American Mineralogist, 88, 639–646, https://doi.org/10.2138/am-2003-0417.

Konecke, B.A., Fiege, A., Simon, A.C., Parat, F., and Stechern, A. (2017) Co-variability of S^{6+}, S^{4+}, and S^{2-} in apatite as a function of oxidation state: Implications for a new oxybarometer. American Mineralogist, 102, 548–557, https://doi.org/10.2138/am-2017-5907.

Konecke, B.A., Fiege, A., Simon, A.C., Linsler, S., and Holtz, F. (2019) An experimental calibration of a sulfur-in-apatite oxybarometer for mafic systems. Geochimica et Cosmochimica Acta, 265, 242–258, https://doi.org/10.1016/j.gca.2019.08.044.

Laputina, I.P., Batyrev, V.A., and Yakushev, A.I. (1999) A new EPMA technique for determination of rare earth elements with the use of automated peak-overlap and modelled background corrections. Journal of Analytical Atomic Spectrometry, 14, 465–469, https://doi.org/10.1039/A806828C.

Mariano, A.N. and King, P.J. (1975) Europium-activated cathodoluminescence in minerals. Geochimica et Cosmochimica Acta, 39, 649–660, https://doi.org/10.1016/0016-7037(75)90008-3.

Marks, M.A.W., Wenzel, T., Whitehouse, M.J., Loose, M., Zack, T., Barth, M., Worgard, L., Krasz, V., Eby, N., Stosnach, H., and others. (2012) The volatile inventory (F, Cl, Br, S, C) of magmatic apatite: An integrated analytical approach. Chemical Geology, 291, 241–255, https://doi.org/10.1016/j.chemgeo.2011.10.026.

McCubbin, F.M., Steele, A., Hauri, E.H., Nekvasil, H., Yamashita, S., and Hemley, R.J. (2010a) Nominally hydrous magmatism on the Moon. Proceedings of the National Academy of Sciences, 107, 11223–11228, https://doi.org/10.1073/pnas.1006677107.

McCubbin, F.M., Steele, A., Nekvasil, H., Schnieders, A., Rose, T., Fries, M., Carpenter, P.K., and Jolliff, B.L. (2010b) Detection of structurally bound hydroxyl in fluorapatite from Apollo Mare basalt 15058,128 using TOF-SIMS. American Mineralogist, 95, 1141–1150, https://doi.org/10.2138/am.2010.3448.

McCubbin, F.M., Jolliff, B.L., Nekvasil, H., Carpenter, P.K., Zeigler, R.A., Steele, A., Elardo, S.M., and Lindsley, D.H. (2011) Fluorine and chlorine abundances in lunar apatite: Implications for heterogenous distributions of magmatic volatiles in the lunar interior. Geochimica et Cosmochimica Acta, 75, 5073–5093, https://doi.org/10.1016/j.gca.2011.06.017.

Pan, Y. and Fleet, M.J. (2002) Composition of the apatite-group minerals: Substitution mechanisms and controlling factors. Reviews in Mineralogy and Geochemistry, 48, 13–49, https://doi.org/10.2138/rmg.2002.48.2.

Patiño Douce, A. and Roden, M. (2006) Apatite as a probe of halogen and water fugacities in the terrestrial planets. Geochimica et Cosmochimica Acta, 70, 3173–3196. https://doi.org/10.1016/j.gca.2006.03.016.

Paton, C., Woodhead, J.D., Hellstrom, J.C., Hergt, J.M., Greig, A., and Maas, R. (2010) Improved laser ablation U-Pb zircon geochronology through robust downhole fractionation correction. Geochemistry, Geophysics, Geosystems, 11, https://doi.org/10.1029/2009GC002618.

Paton, C., Hellstrom, J., Paul, B., Woodhead, J., and Hergt, J. (2011) Iolitie: Freeware for the visualisation and processing of mass spectrometric data. Journal of Analytical Atomic Spectrometry, 26, 2508–2518, https://doi.org/10.1039/C1JA10172B.

Piccoli, P.M. and Candela, P.A. (2002) Apatite in igneous systems. Reviews in Min-

eralogy and Geochemistry, 48, 255-292. https://doi.org/10.2138/rmg.2002.48.6.
Plank, T. and Langmuir, C.H. (1998) The chemical composition of subducting sediment and its consequences for the crust and mantle. Chemical Geology, 145, 325–394, https://doi.org/10.1016/S0009-2541(97)00150-2.
Prowatke, S. and Klemme, S. (2006) Trace element partitioning between apatite and silicate melts. Geochimica et Cosmochimica Acta, 70, 4513–4527, https://doi.org/10.1016/j.gca.2006.06.162.
Rakovan, J., Newville, M., and Sutton, S. (2001) Evidence of heterovalent europium in zoned Llallagua apatite using wavelength dispersive XANES. American Mineralogist, 86, 697–700, https://doi.org/10.2138/am-2001-5-610.
Ravel, B. and Newville, M. (2005) ATHENA, ARTEMIS, HEPHAESTUS: Data analysis for X-ray absorption spectroscopy using IFEFFIT. Journal of Synchrotron Radiation, 12, 537–541, https://doi.org/10.1107/S0909049505012719.
Reed, R.J.B. and Buckley, A. (1998) Rare-earth element determination in minerals by electron-probe microanalysis: Application of spectrum synthesis. Mineralogical Magazine, 62, 1–8, https://doi.org/10.1180/002646198547404.
Rhodes, G. and Hubbard, N.J. (1973) Chemistry, classification, and petrogenesis of Apollo 15 mare basalts. Proceedings of the 4th Lunar Science Conference, 2, 1127–1148.
Robinson, K.L., Barnes, J.J., Villeneuve, J., Johnson, D., Deloule, E., Franchi, I.A., and Anand, M. (2017) Ion Microprobe Analyses of Trace Elements in Lunar Apatites. In: 48th Lunar and Planetary Science Conference, 20–24 March 2017, The Woodlands, Houston, Texas.
Roeder, P.L., MacArthur, D., Ma, X.-P., Palmer, G.R., and Mariano, A.N. (1987) Cathodoluminescence and microprobe study of rare-earth elements in apatite. American Mineralogist, 72, 801–811.
Sato, M. (1976) Oxygen fugacity values of some Apollo 16 and 17 rocks. In Lunar and Planetary Science Conference, vol. 7, 758 p.
Schnetzler, C.C. and Philpotts, A.J. (1970) Partition coefficient of rare earth elements between igneous matrix material and rock-forming mineral phenocrysts-II. Geochimica et Cosmochimica Acta, 34, 331–340, https://doi.org/10.1016/0016-7037(70)90110-9.
Shearer, C.K., Papike, J.J., Burger, P.V., Sutton, S.R., McCubbin, F.M. and Newville, M. (2011) Direct determination of europium valence state by XANES in extraterrestrial merrillite: implications for REE crystal chemistry and martian magmatism. American Mineralogist, 96, 1418–1421, https://doi.org/10.2138/am.2011.3860.
Shearer, C.K., Papike, J.J., and Karner, J.M. (2006) Pyroxene europium valence oxybarometer: Effects of pyroxene composition, melt composition, and crystallization kinetics. American Mineralogist, 91, 1565–1573, https://doi.org/10.2138/am.2006.2098.
Smythe, D.J. and Brenan, J.M. (2016) Magmatic oxygen fugacity estimated using zircon-melt partitioning of cerium. Earth and Planetary Science Letters, 453, 260–266, https://doi.org/10.1016/j.epsl.2016.08.013.
Strasheim, A., Coetzee, J.H.J., Jackson, P.F.S., Strelow, F.W.E., Wybenga, F.T., Gricius, A.J., and Kokot, M.L. (1972) Analysis of lunar samples 15065, 15301, and 15556, with isotopic data for $_7$Li/$_6$Li. In J.W. Chamberlain and C. Watkins, Eds., The Apollo 15 Lunar Samples, 257–259. The Lunar Science Institute.
Tartèse, R., Anand, M., Barnes, J.J., Starkey, N.A., Franchi, I.A., and Sano, Y. (2013) The abundance, distribution, and isotopic composition of Hydrogen in the Moon as revealed by basaltic lunar samples: Implications for the volatile inventory of the Moon. Geochimica et Cosmochimica Acta, 122, 58–74, https://doi.org/10.1016/j.gca.2013.08.014.
Taylor, S.R. (1982) Planetary science: A lunar perspective, Lunar and Planetary Institute, vol. 3303.
Taylor, S.R., Gorton, M.P., Muir, P., Nance, W.B., Rudowski, R.R., and Ware, N. (1973) Composition of the Descartes region, lunar highlands. Geochimica et Cosmochimica Acta, 37, 2665–2683, https://doi.org/10.1016/0016-7037(73)90271-8.
Tollari, N., Toplis, M.J., and Barnes, S.-J. (2006) Predicting phosphate saturation in silicate magmas: An experimental study of the effects of melt composition and temperature. Geochimica et Cosmochimica Acta, 70, 1518–1536, https://doi.org/10.1016/j.gca.2005.11.024.
Trail, D., Watson, E.B., and Tailby, N.D. (2011) The oxidation state of Hadean magmas and implications for early Earth's atmosphere. Nature, 480, 79–82, https://doi.org/10.1038/nature10655.
——— (2012) Ce and Eu anomalies in zircon as proxies for the oxidation state of magmas. Geochimica et Cosmochimica Acta, 97, 70–87, https://doi.org/10.1016/j.gca.2012.08.032.
Trail, D., Tailby, N.D., Lanzirotti, A., Newville, M., Thomas, J., and Watson, E.B. (2015) Redox evolution of silicic magmas: Insights from XANES measurements of Ce valence in Bishop Tuff zircons. Chemical Geology, 402, 77–88, https://doi.org/10.1016/j.chemgeo.2015.02.033.
Wadhwa, M. (2008) Redox conditions on small bodies, the Moon and Mars. Reviews in Mineralogy and Geochemistry, 68, 493–510, https://doi.org/10.2138/rmg.2008.68.17.
Wakita, H., Schmitt, R.A., and Rey, P. (1970) Elemental abundances of major, minor and trace elements in Apollo 11 lunar rocks, soil and core samples. Proceedings of the Apollo 11 Lunar Science Conference. 2, 1685–1717.
Walker, D., Grove, T.L., Longhi, J., Stolper, E.M., and Hays, J.F. (1973) Origin of lunar feldspathic rocks. Earth and Planetary Science Letters, 20, 325–336, https://doi.org/10.1016/0012-821X(73)90006-X.
Wänke, H. Palme, H., Baddenhausen, H., Dreibus, G., Jagoutz, E., Kruse, H., Palme, C., Spettel, B., Teschke, F., and Thacker, R. (1975) New data on the chemistry of lunar samples: Primary matter in the lunar highlands and the bulk composition of the moon. Proceedings of the 6th Lunar Science Conference, 2, 1313–1340.
Warren, P.H., Afiattalab, F., and Wasson, J.T. (1978) Investigation of unusual KREEPy samples: Pristine rock 15386, Cone Crate soil fragments 14143, and 12023, a Typical Apollo 12 soil. Proceedings of the 9th Lunar and Planetary Science Conference, 653–660.
Watson, E.B. (1979) Apatite saturation in basic to intermediate magmas. Geophysical Research Letters, 6, 937–940, https://doi.org/10.1029/GL006i012p00937.
Watson, E.B. and Green, T.H. (1981) Apatite/liquid partition coefficients for the rare earth elements and strontium. Earth and Planetary Science Letters, 56, 405–421, https://doi.org/10.1016/0012-821X(81)90144-8.
Watson, E.B. and Harrison, T.M. (1983) Zircon saturation revisited: Temperature and composition effects in a variety of crustal magma types. Earth and Planetary Science Letters, 64, 295–304, https://doi.org/10.1016/0012-821X(83)90211-X.
Webster, J.D. and Piccoli, P.M. (2015) Magmatic apatite: a powerful, yet deceptive, mineral. Elements, 11, 177–182, https://doi.org/10.2113/gselements.11.3.177.
Xing, L., Trail, D., and Watson, E.B. (2013) Th and U partitioning between monazite and felsic melt. Chemical Geology, 358, 46–53, https://doi.org/10.1016/j.chemgeo.2013.07.009.

Manuscript received November 14, 2021
Manuscript accepted March 2, 2022
Accepted manuscript online May 11, 2022
Manuscript handled by Justin Filiberto

Endnote:

[1]Deposit item AM-23-58388, Online Materials. Deposit items are free to all readers and found on the MSA website, via the specific issue's Table of Contents (go to http://www.minsocam.org/MSA/AmMin/TOC/2023/May2023_data/May2023_data.html).